

Multimessenger Emission from the Accretion-Induced Collapse of White Dwarfs

Luís Felipe Longo Micchi^{1,2,3,4}, David Radice^{* 2,3,5}, and Cecilia Chirenti^{6,7,8,9}

¹ Center for Natural and Human Sciences, Universidade Federal do ABC, Santo André, SP 09210-170, Brazil

² Institute for Gravitation & the Cosmos, The Pennsylvania State University, University Park, PA 16802, USA

³ Department of Physics, The Pennsylvania State University, University Park, PA 16802, USA

⁴ Theoretisch-Physikalisches Institut, Friedrich-Schiller-Universität Jena, 07743, Jena, Germany

⁵ Department of Astronomy & Astrophysics, The Pennsylvania State University, University Park, PA 16802, USA

⁶ Department of Astronomy, University of Maryland, College Park, Maryland 20742, USA

⁷ Astroparticle Physics Laboratory NASA/GSFC, Greenbelt, Maryland 20771, USA

⁸ Center for Research and Exploration in Space Science and Technology

⁹ Center for Mathematics, Computation and Cognition, UFABC, Santo André-SP, 09210-170, Brazil

Submitted to Monthly Notices of the Royal Astronomical Society on June 14th, 2023

ABSTRACT

We present fully general-relativistic three-dimensional numerical simulations of accretion-induced collapse (AIC) of white dwarfs (WDs). We evolve three different WD models (nonrotating, rotating at 80% and 99% of the Keplerian mass shedding limit) that collapse due to electron capture. For each of these models, we provide a detailed analysis of their gravitational waves (GWs), neutrinos and electromagnetic counterpart and discuss their detectability. Our results suggest that fast rotating AICs could be detectable up to a distance of 8 Mpc with third-generation GW observatories, and up to 1 Mpc with LIGO. AIC progenitors are expected to have large angular momentum due to their accretion history, which is a determining factor for their stronger GW emission compared to core-collapse supernovae (CCSNe). Regarding neutrino emission, we found no significant difference between AICs and CCSNe. In the electromagnetic spectrum, we find that AICs are two orders of magnitude fainter than type Ia supernovae. Our work places AICs as realistic targets for future multimessenger searches with third generation ground-based GW detectors.

Key words: White Dwarf – Gravitational Collapse – Gravitational Waves – Neutrino – Multi-messenger Astronomy

1 INTRODUCTION

Since the first detection of gravitational waves (GWs) was performed by the LIGO collaboration (Abbott et al. 2016), we have faced a great expansion of multimessenger astronomy (MMA). Commonly discussed sources for MMA are compact binary mergers and events involving stellar collapse. Among the stellar collapse events, perhaps the most studied cases in the literature are type Ia supernovae (SNeIa) and core collapse supernovae (CCSNe). Far from being the only types of stellar explosion, other physical processes can be behind the explosion mechanism of a collapsing star. In this paper, we focus on accretion-induced collapse (AIC) of white dwarfs (WDs).

WDs are compact stars supported by electron degeneracy pressure (Chandrasekhar 1931b). In order for gravitational collapse to take place, the total gravitational mass of the WD has to exceed the Chandrasekhar mass, $M_{\text{Chand.}} \approx 1.44M_{\odot}$ (Chandrasekhar 1931b,a). Nomoto (1986) studied the final fate of accreting WDs based on their accretion rate, initial total mass, and composition. If a low-mass ($M \lesssim 1.2M_{\odot}$) C-O WD faces an intense accretion history

($10^{-7}M_{\odot}\text{yr}^{-1} \lesssim \dot{M} \lesssim 10^{-5}M_{\odot}\text{yr}^{-1}$), then the star is likely to undergo a carbon deflagration and it will detonate as an SNIa, leaving no remnant behind (see also the work of Shen et al. 2009; Shen & Bildsten 2009; Moore et al. 2013). The AIC happens if a high mass ($M \gtrsim 1.2M_{\odot}$) O+Ne+Mg or Si+O WD accretes slowly ($\dot{M} \lesssim 10^{-9}M_{\odot}\text{yr}^{-1}$), leading the star to collapse and form a neutron star (NS). The different outcomes, SNIa explosion or AIC, depend on the WD composition since lower-Z compositions release a larger amount of energy during burning.

AIC events have been connected to the nucleosynthesis of very rare neutron-rich heavy elements, such as ⁶²Ni, ⁶⁶Zn, ⁶⁸Zn, ⁸⁷Rb and ⁸⁸Sr. Fryer et al. (1999) studied the r-process in AICs to constrain their event rate given the cosmological abundances of these elements and estimated between 1 and 200 events per 10⁶ years per galaxy.

AICs have also been invoked to explain a plethora of different astrophysical phenomena. AICs are expected to have highly rotating progenitors due to their accretion history (Uenishi et al. 2003; Piersanti et al. 2003a,b; Saio & Nomoto 2004; Yoon & Langer 2004b, 2005; Kashyap et al. 2018), as they could form either in a double degenerate case (WD-WD merger) or a single degenerate case (a WD

* Alfred P. Sloan fellow

Simulation	ρ_0 [g cm ⁻³]	Temp. [MeV]	M [M_\odot]	$M_{\text{bar.}}$ [M_\odot]	R [km]
rot	9.95×10^9	0.01	1.52	1.53	1.93×10^3
rot_ar075	9.95×10^9	0.01	1.51	1.53	1.71×10^3
nrot	9.95×10^9	0.01	1.45	1.47	1.33×10^3
Simulations	J [g cm ² s ⁻¹]	T/W	Ω [Hz]	Ω_{Kepler} [Hz]	a_r
rot	3.26×10^{49}	1.49×10^{-2}	5.28	5.30	0.66
rot_ar075	3.08×10^{49}	1.37×10^{-2}	5.09	6.38	0.75
nrot	0	0	0	9.03	1.00

Table 1. Initial conditions for the three simulations performed during this work. The parameters are as follows: ρ_0 : central baryonic density, Temp.: central temperature, $M_{\text{bar.}}$: baryonic mass, M : gravitational mass, R : stellar equatorial radius, J : total angular momentum, $\frac{T}{W}$: the ratio between rotational and gravitational energy, Ω : rotational frequency, Ω_{Kepler} : the Keplerian angular velocity at the equator on the surface of the star, a_r : ratio between the polar radius and the equatorial radius of the star. The rot_ar075 model spins at $0.8 \Omega_{\text{Kepler}}$ and the rot model spins close to the break-up limit at $0.99 \Omega_{\text{Kepler}}$.

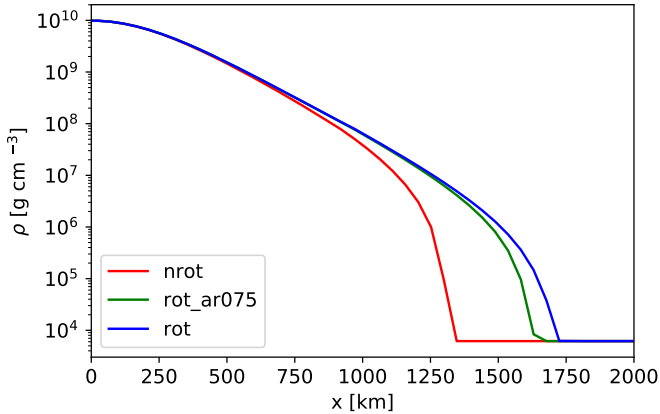


Figure 1. Initial density profile in the equatorial plane. For fixed density ρ_0 , rotating stars have larger radii and higher total masses.

accreting from a companion star that overflows its Roche lobe).¹ Therefore angular momentum is expected to play a major role in their GW emission (Dimmelmeier et al. 2008; Shibagaki et al. 2021). Additionally, AICs could form magnetars as their remnants, possibly powering gamma-ray bursts (Yi & Blackman 1998; Metzger et al. 2008; Perley et al. 2009). Continued accretion after the formation of the NS remnant from the AIC could lead to the formation of a millisecond pulsar or low-mass X-ray binary (Hurley et al. 2010; Tauris et al. 2013; Ablimit 2022; Wang et al. 2022).

Fast radio bursts (FRBs) have also been tentatively connected with AICs. According to Waxman (2017) and Margalit et al. (2019), the properties of FRB 121102 and FRB 180924 are consistent with those of a magnetized NS formed in a weak stellar explosion, which could for example be an AIC or a binary WD merger.

AIC simulations have been performed by different groups. Fryer et al. (1999) employed 1D and 2D simulations to determine the composition of the ejected material and concluded that an AIC does not produce enough nickel to explain the formation of a SNIa. Dessart et al. (2006) performed studies in 2D Newtonian gravity and showed that AIC events with no magnetic fields should display low ejecta mass ($M_{\text{ej.}} \sim 10^{-3} M_\odot$) with an entropy ranging between 20 and 50 k_B /baryon and explosion energy of $\lesssim 10^{50}$ erg. When magnetic fields are included, Dessart et al. (2007) reported, among other differences, an increase in ejecta mass by a factor of 100 ($M_{\text{ej.}} \sim 0.1 M_\odot$). More

¹ A third formation channel for AICs was proposed by Ablimit et al. (2022), in which the WD enters a common envelope phase with its companion (core-merger-induced collapse).

recent 2D simulations including general relativity (GR) effects were performed by Abdikamalov et al. (2010), who predicted that AICs are subjected to low $\frac{T}{|W|}$ -type dynamical instabilities (Shibata et al. 2000; Centrella et al. 2001; Shibata et al. 2003; Ott et al. 2005; Ou & Tohline 2006; Cerdá-Durán et al. 2007), due to the existence of a corotating point inside the star (Watts et al. 2004; Saijo & Yoshida 2006). Finally, GW signals generated by the AIC of dark matter admixed WDs have been studied by Chan et al. (2023), who find that dark matter accumulated in the WD can have an impact on the GW emission.

In this paper, we perform fully general relativistic 3D simulations of AIC of rotating WDs. Our simulations include an M1 grey neutrino radiation transport scheme via the WhiskyTHC code (Radice et al. 2022), which is implemented within the Einstein Toolkit (Löffler et al. 2012). This paper is organized as follows. The numerical setup and initial data are presented in Section 2. Our results are discussed in the following Sections: collapse and post-bounce dynamics of the AIC (Section 3), expected gravitational radiation emission of an AIC event (Section 4), effects of the weak (im)balance of the nucleons and how it gives rise to the neutrino flux (Section 5) and properties of the ejected material and estimates for the electromagnetic emission (Section 6). In Section 7 we present our conclusions.

2 NUMERICAL METHODS

2.1 Numerical Setup

In our numerical setup, we ignore the path that brought the WD to the brink of collapse and consider only an isolated WD, with initial conditions set to induce the AIC (see Sec. 2.2).

Our models are evolved with the WhiskyTHC code (Radice & Rezzolla 2012; Radice et al. 2013, 2014, 2016, 2018), which uses the Einstein Toolkit framework (Löffler et al. 2012). More specifically, the space-time evolution is executed via the CTGamma thorn (Pollney et al. 2011; Reisswig et al. 2013), which solves the Einstein equations in the Z4c formulation. The hydrodynamical quantities are calculated with WhiskyTHC, which implements high-order convergence schemes for general relativistic hydrodynamics and contains a moment-based neutrino transport scheme (Radice et al. 2022). For the time evolution, we use a finite difference Runge-Kutta scheme with (spatially-dependent) fixed time steps set by a CFL factor of 0.15, which defines the ratio between the temporal and spatial resolution of the grid. The spatial grid is constructed by the Carpet thorn (Schnetter et al. 2004). An AMR grid is constructed by requiring 10 logarithmically (base 2) evenly spaced resolution levels. The outermost grid has its x and y coordinates within ± 6284.9 km, while $0 < z < 6284.9$ km due to the imposed symmetry with respect to the xy plane. All refinement levels respect

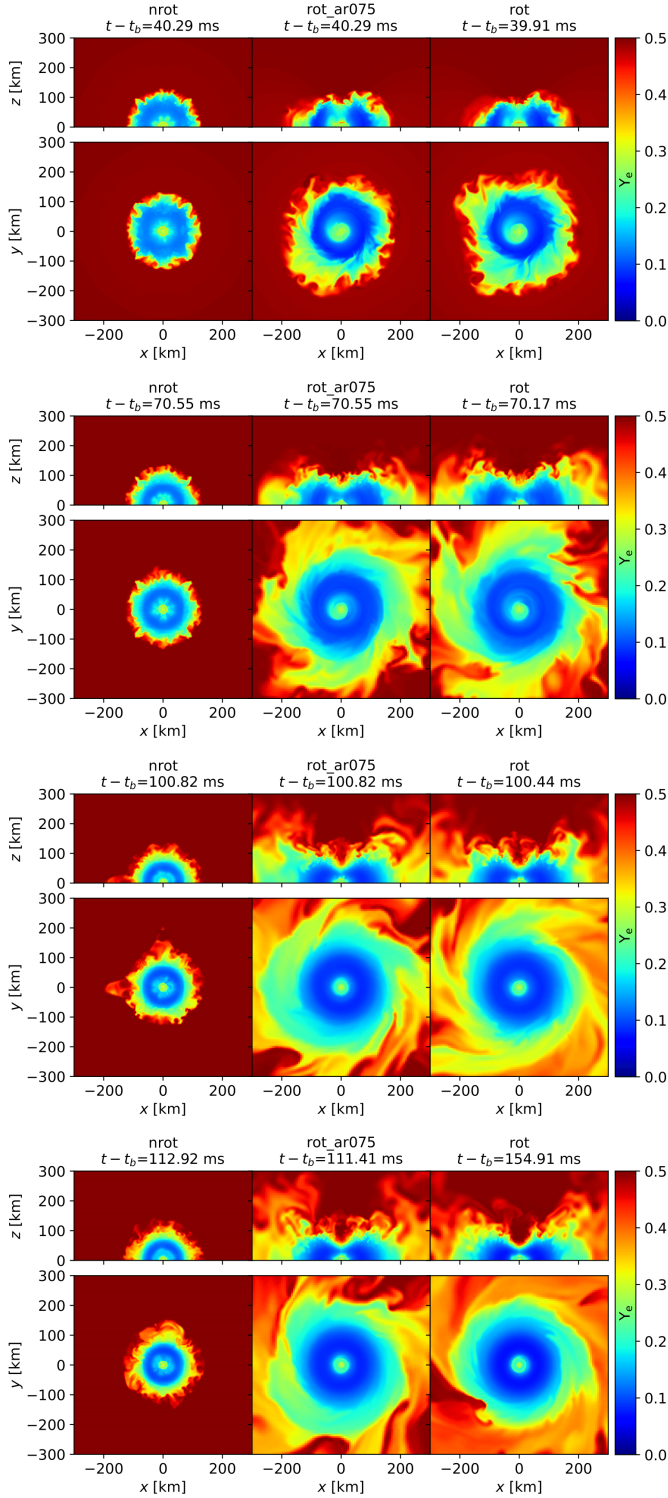


Figure 2. Electron fraction Y_e in the equatorial and meridional planes. Most of the low Y_e material ($Y_e \lesssim 0.2$) remains bound to the central region with $r < 100$ km. As the dense spiral arms travel outwards, the material becomes electron rich again ($Y_e \gtrsim 0.3$). The region with low electron fraction is larger for the rotating cases. Both *rot* and *rot_ar075* display a torus-like morphology, while *nrot* is closer to spherical symmetry. The slight increase in Y_e towards the center of the star is due to the fact that electron captures are suppressed by Pauli blocking.

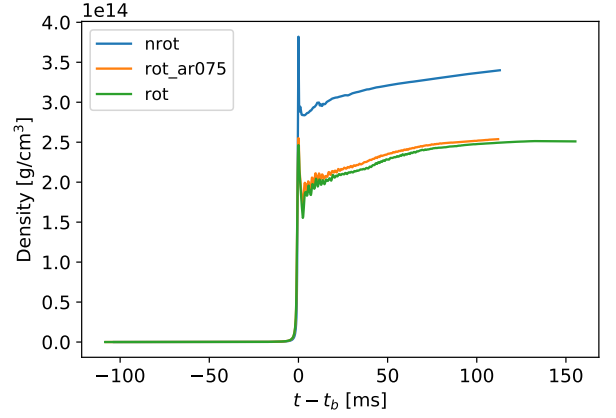


Figure 3. Time evolution of the central density of the star. The time of bounce (t_b) is marked by the first local maximum of $\rho_0(t)$. After the bounce, the central density increases due to the collapse of the outer layers. The oscillations visible at early times after the bounce represent perturbation modes of the remnant PNS (Fuller et al. 2015; Rodriguez et al. 2023). Note the clear effect of rotation in decreasing the central density, as the centrifugal force tends to spread the material to larger radius, see also Fig. 1.

this reflection requirement and contain $128 \times 128 \times 64$ grid points. The grid resolution in the finest refinement level covering the protoneutron star (PNS) remnant is 0.369 km. The GWs presented here were obtained via the *WeylScal4* thorn, which evolves and extracts the Weyl scalar at a finite radius. We cross-validated the GW strain found with *WeylScal4* against the results achieved by the *ZelmaniQuadWaveExtract* thorn, which computes the GW in the quadrupole approximation at radial infinity.

2.2 Initial Data

Different evolutionary paths to an AIC could affect, for example, the spin of the WD. We label our simulations with a_r , the ratio between the polar and equatorial radii of the progenitor WDs. Our models are *nrot*, *rot_ar075*, and *rot* for the non-rotating, fast rotating, and maximally rotating progenitors, corresponding to values of $a_r = 1, 0.75$, and 0.66 , respectively. All of the models are rigidly rotating at the beginning of the simulations. More information about their initial properties is in Table 1. The maximally rotating case is very close to the maximum angular momentum supported by the initial WD before being disrupted by the centrifugal force and spins at 99% of the Keplerian mass-shedding frequency.

All of the three progenitors have the same initial baryonic central density ($\rho_0 = 9.95 \times 10^9$ g/cm³ because this value is argued by Abdikamalov et al. (2010), Nomoto & Kondo (1991), Yoon & Langer (2004a), and Dessart et al. (2006) to be representative of a WD in the verge of collapse) and temperature ($T_0 = 0.01$ MeV). Initial data were generated with the *RNSID* thorn (Stergioulas & Friedman 1995). The equation of state used in this work is the LS220 EOS proposed by Lattimer & Swesty (1991), which assumes nuclear statistical equilibrium and relies on a compressible liquid-drop model for the nuclei, including effects of interactions and degeneracy of the nucleons outside nuclei. The initial central values (ρ_0, T_0) are chosen to emulate configurations on the verge of collapse, which requires that the initial mass of the WD should be greater than the Chandrasekhar limit. The slightly different values of initial mass are a consequence of the extra support provided by the initial rotation and the initial density profiles are shown in Fig. 1.

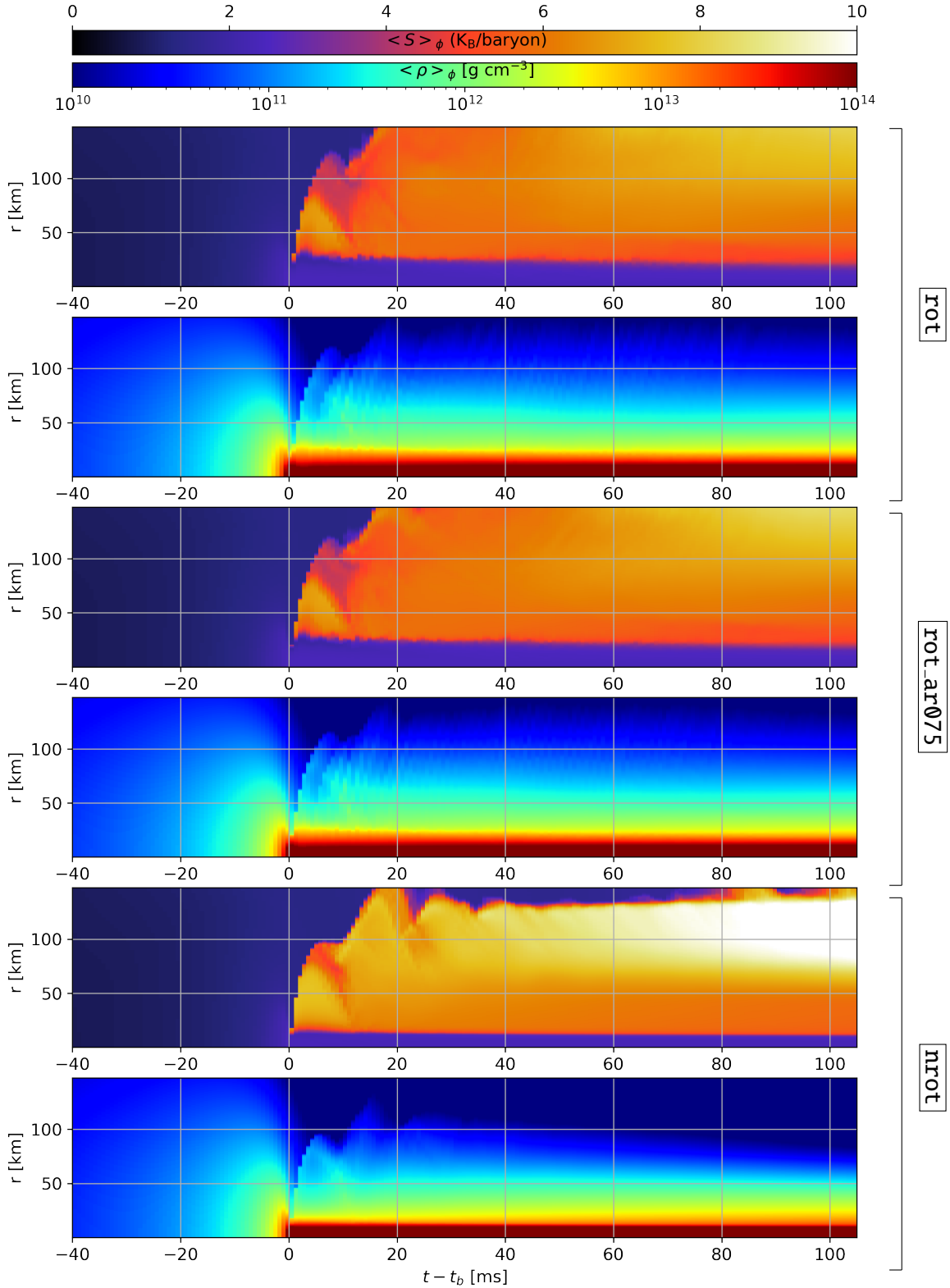


Figure 4. Angular average of the equatorial entropy S and density ρ profiles throughout the evolution of the AIC. The regions with low density and large entropy are correlated. The high-entropy material pushes the fluid outwards (expanding to lower densities) due to the convective instability. The large increase of entropy occurs shortly after the bounce, as the shock starts to move away from the center of the star. The large density region ($r \lesssim 25$ km) is the PNS core. The stalled shock is seen in the `nrot` model as the large entropy material ceases to expand at later times ($t - t_b \gtrsim 40$ ms).

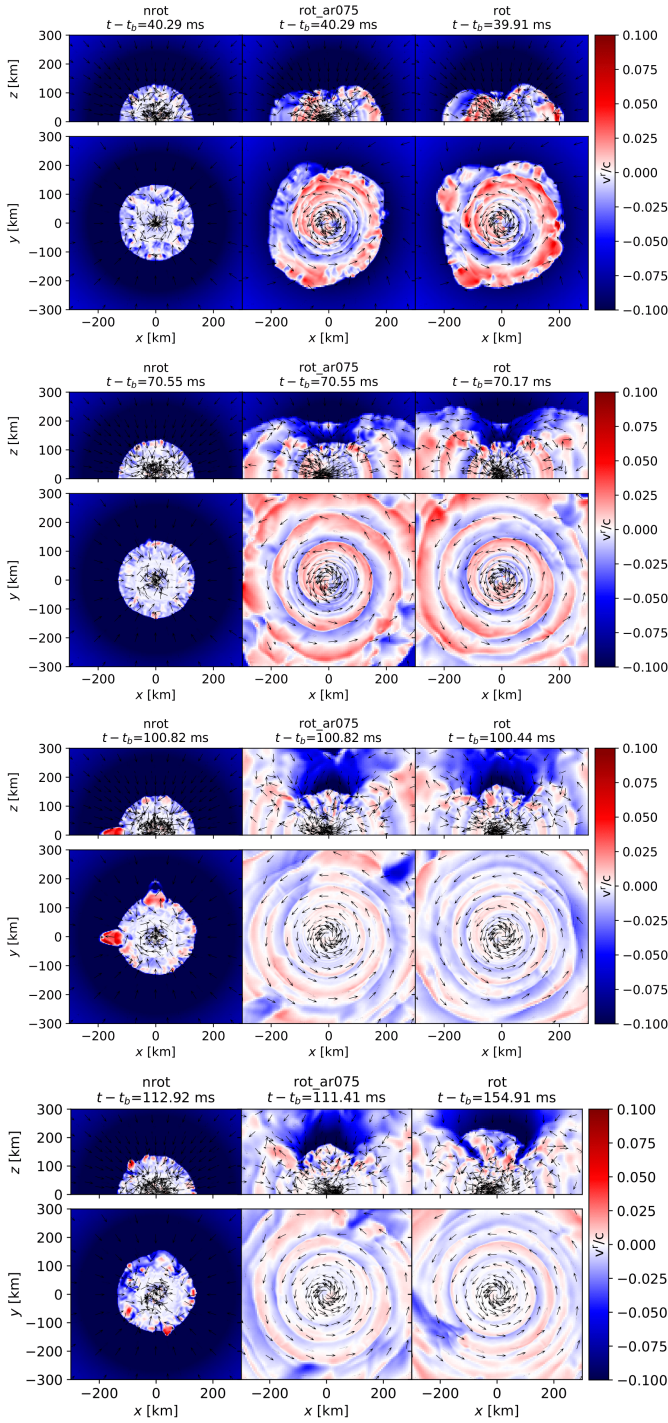


Figure 5. Velocity profile of the fluid. The color scheme shows the radial velocity, while the arrows display the direction of the motion. Rotation plays a key role in the explosion, as the shock in the nonrotating case seems to stall very early in the evolution.

The maximum mass that can be supported in a cold², non-rotating

² The temperature of the star is well below the Fermi energy of its ultra-relativistic electrons. As the star is typically at $\sim 10^6 - 10^7$ K and $E_F \sim 10^9$ K the $T = 0$ approximation is usually very accurate.

WD composed of a Fermi gas of protons, neutrons, and ultra-relativistic electrons is given by (Glendenning 2000)

$$M_{\max} \approx 5.87 \times Y_e^2 \times M_{\odot}, \quad \text{where } Y_e \equiv \frac{n_e}{n_p + n_n} \quad (1)$$

is the electron fraction. The number densities of electrons, protons, and neutrons are represented by n_e , n_p , and n_n , respectively. Assuming charge neutrality ($n_e = n_p$) and a C+O or O+Ne+Mg composition ($Y_e = 0.5$), we find $M_{\max} \sim 1.46 M_{\odot}$, consistent with our non-rotating model in 1.

Numerically, it is necessary to impose a low-density atmosphere around the star. In practice, we do this by setting low values for the density, neutrino number density, and neutrino energy density (for all neutrino flavors) outside of the star: $\rho_{\text{atm}} = 6.18 \times 10^3 \text{ g/cm}^3$, $n_{\nu, \text{atm}} = 3.10 \times 10^{-31} \text{ cm}^{-3}$, and $E_{\nu, \text{atm}} = 5.55 \times 10^8 \text{ erg/cm}^3$, respectively.

3 COLLAPSE DYNAMICS

The electron fraction inside a collapsing WD decreases as electron capture takes place, driven by the inverse β -decay: $p + e^- \rightarrow n + \nu_e$. In our code, we describe this process with the effective deleptonization scheme developed by Liebendörfer (2005). In Fig. 2, we show the time evolution of the electron fraction. In the beginning of the collapse stage (not shown in Fig. 2), we have $Y_e \sim 0.5$ everywhere inside the star. The deleptonization process starts in the stellar core ($\rho \sim 10^{10} \text{ g/cm}^3$ in the beginning of our simulations) and the electron degeneracy pressure, that initially supports the star against gravitational collapse, diminishes drastically. Consequently, the star enters the *collapse* stage and becomes increasingly denser, as seen in Figs. 3 and 4.

The collapse phase is mainly characterized by purely ingoing fluid motion. After achieving central densities comparable to the nuclear saturation density ($\rho_c \sim 10^{14} \text{ g/cm}^3$), the stellar core stiffens significantly. The central density achieves its first local maximum (see Fig. 3) followed by an abrupt relaxation, marking the time of *bounce* (t_b) of the core. At this time, Y_e achieves values of ≈ 0.25 in the core. In this context, the collapse phase refers to $t - t_b < 0$, whereas the *post-bounce* phase refers to $t - t_b > 0$. When the core bounces, it injects an enormous amount of kinetic energy in the surrounding stellar fluid, which starts an outgoing motion. Fig. 5 shows the velocity profile of the stellar fluid for $t - t_b > 0$. Besides the larger scale outgoing motion in the post-bounce phase, a smaller amount of fluid steadily accretes to the core as the AIC evolves. During the early times of the post-bounce phase it is possible to see oscillations in the density profile of the stellar core (see Fig. 3), which are associated with the quasi-normal mode oscillations of the remnant PNS.

The rotation of the progenitor WD has a striking effect in the late evolution of the AIC, shown in Fig. 5. Shortly after the bounce, some of the infalling material starts traveling in the opposite direction, achieving mildly relativistic velocities ($v_r \lesssim 0.1c$) for the rotating progenitors. However, the shock of the nrot model stalls at $t - t_b \approx 40$ ms. In this case, the shock ceases to propagate radially at a distance of ≈ 100 km from the center, showing no sign of a shock revival for the remaining duration of the simulation. The stronger shocks seen in the rot and nrot_ar075 models are enhanced (compared with the stalled shock in nrot) by the kinetic energy of the rotating stars.

While the AIC from a non-rotating progenitor maintains approximate spherical symmetry at all times, the models with rotating progenitors display spiral arms that propagate outwards. These spiral

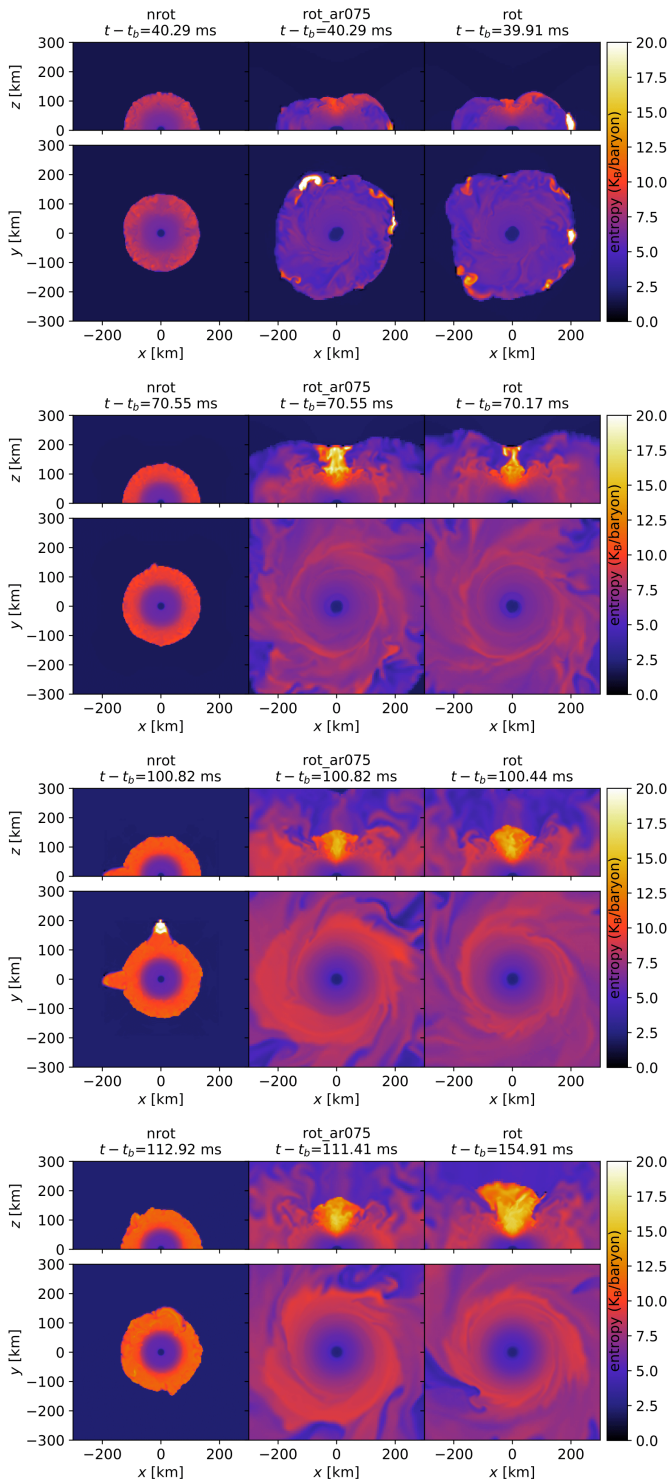


Figure 6. Entropy profile of the central part of the collapsing WD. The high entropy material is related to the shock front, while the center of the PNS remains with low entropy, see also Fig. 5. In the nrot model, which presents a stalled shock, the high entropy material remains contained to $70 \text{ km} < r < 150 \text{ km}$ and displays systematically higher entropy than the cases with rotating progenitors. In the rot_ar075 and rot models, the high entropy material keeps expanding and there is ejection of high entropy material from the pole, see also Fig. 5.

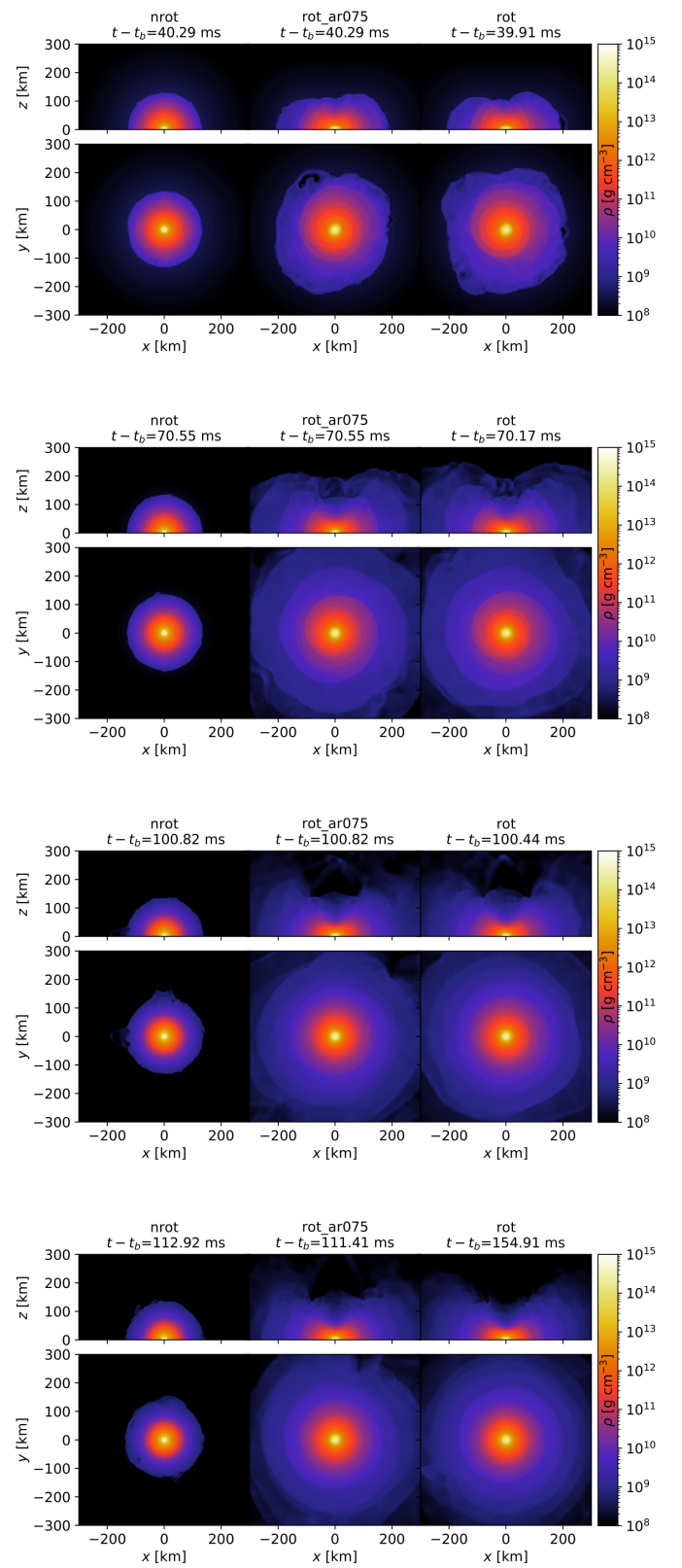


Figure 7. Density in the equatorial and meridional planes. The rot_ar075 and rot models present a successful explosion, whereas the shock is stalled for the nrot model at $r \approx 100 \text{ km}$. A clear torus-like (expanding) structure appears for rot and rot_ar075.

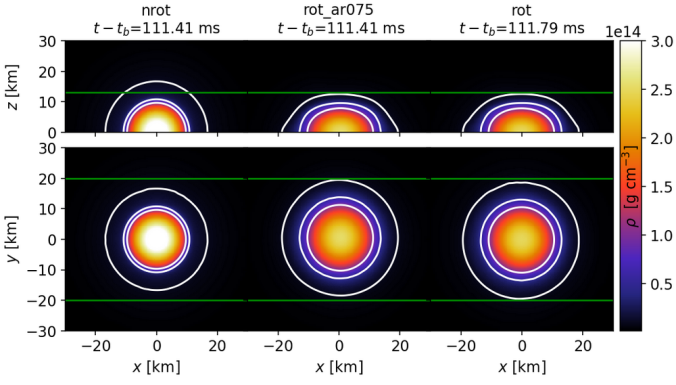


Figure 8. Density profile of the central part of the collapsing WD, the PNS. Here we display the final snapshot of the density field with overlapping isodensity surfaces highlighted in white, representing $1, 5$ and $10 \times 10^{13} \text{ g cm}^{-3}$. The profile of the PNS has already started to settle into a more symmetric configuration. The horizontal green lines are added to aid a visual size comparison: models with initial angular momentum produce larger PNSs.

arms maintain a torus-like morphology throughout the post-bounce phase. The spiral motion of the fluid pushes the low Y_e material away from the center, and as the material expands the electron fraction becomes nearly symmetric again due to e^+ capture associated and ν_e absorption. The material with low electron fraction ($Y_e \lesssim 0.3$) is constrained to the central 100 (200) km for the nrot model (rot_ar075 and rot models).

Comparing Figs. 5 and 6, we can see that the shock fronts display relatively large values of entropy ($S \approx 10 k_B/\text{baryon}$). This effect is even more visible in the polar region, where higher values of entropy ($S \approx 15 k_B/\text{baryon}$) can be seen. There is a cone-like structure in the polar region of models rot and rot_ar075, containing low-density material (see Fig. 7) with symmetric Y_e (Fig. 2), mildly relativistic outgoing velocity ($v \approx 0.08c$, see Fig. 5) and high entropy (Fig. 6), being expelled from the poles. This material is pushed away from the central part of the star by neutrino absorption (see also Section 5.2). This seems to indicate that ejection is favored at the poles in a collimated fashion. In the presence of magnetic fields, these ejections at the poles could facilitate the breaking of field lines, possibly making these regions hot spots for the formation of jets.

Further examination of Fig. 4 confirms that a PNS is left behind a remnant of an AIC. Setting $\rho \sim 10^{11} \text{ g cm}^{-3}$ as the surface of the PNS, we can see that the remnants are contracting (more rapidly for the nrot model). These remnants have extremely dense cores, achieving central densities $\rho_0 \gtrsim 10^{14} \text{ g cm}^{-3}$. Another important property of the PNSs is their electron fraction, which is always smaller than $\lesssim 0.3$ (see Fig. 2).

4 GRAVITATIONAL WAVE EMISSION

The emission of GWs requires the accelerated motion of an asymmetrical (a quadrupole mode or higher) mass distribution. To verify the asymmetry in the mass distribution of our models, we use two independent methods: a visual inspection of the density fluctuations and a mode decomposition of the stellar density profile. First, we compute the angular-averaged relative perturbation of the density profile, defined as:

$$\Delta\rho \equiv \frac{\rho - \langle \rho \rangle_{\phi, \theta}}{\langle \rho \rangle_{\phi, \theta}}, \quad (2)$$

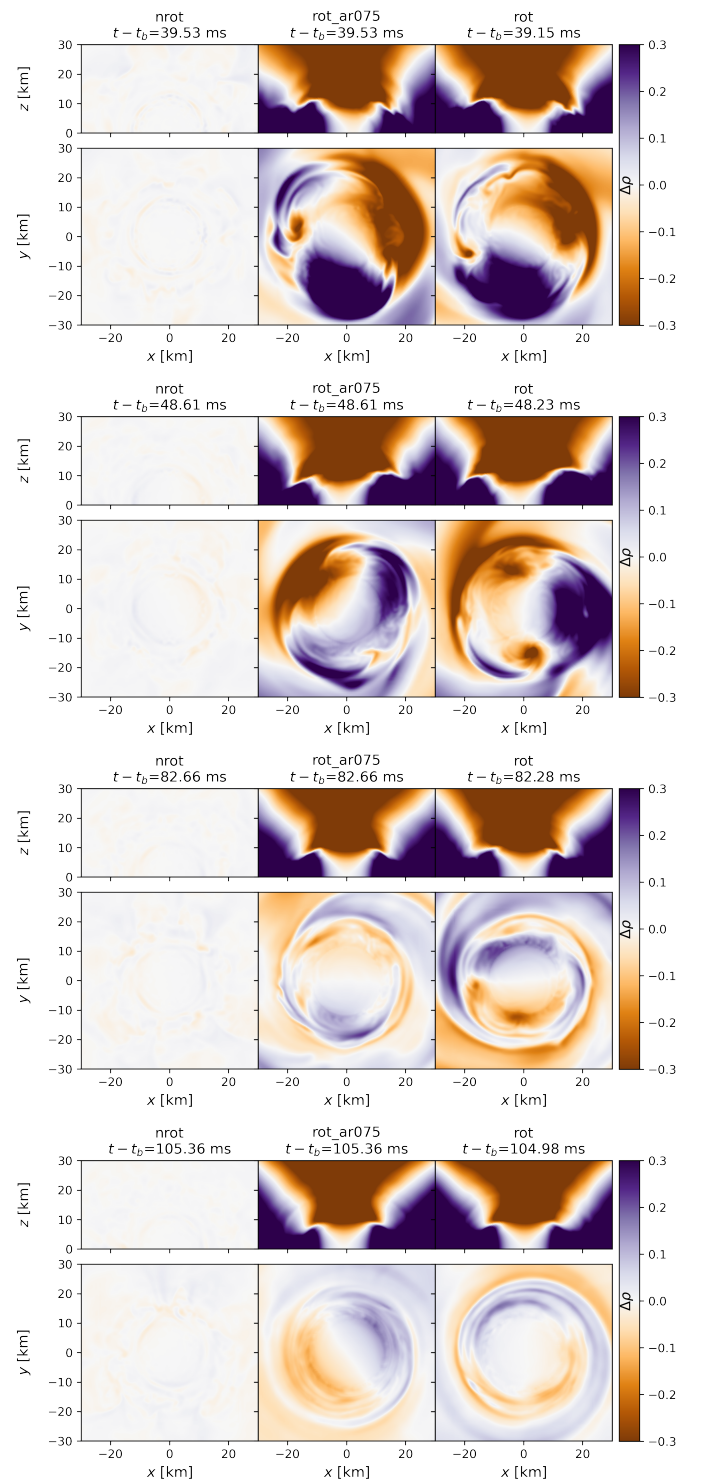


Figure 9. Angular-averaged profile of relative density fluctuations ($\Delta\rho$) in the central part of the collapsing WD, the PNS, shown in the equatorial and meridional planes. Density fluctuations for the nrot model are negligible compared with the cases with a rotating progenitor. For the rot_ar075 and rot models, at early times there is a strong $m = 2$ mode with two overdense regions (in blue) intercalated between two underdense (in gold) regions. At later times the most prominent mass distribution mode is the $m = 1$ where one overdense (in blue) region is diametrically opposed to an underdense (in gold) region. The equatorial plane view shows overdense thick disks in the rot and rot_ar075 models.

where $\langle \rho \rangle_{|\phi, \theta}$ is the angular average in $\phi \equiv \arctan(y/x)$ (when plotting in the xy plane) or $\theta \equiv \arctan(z/r)$ (when plotting the yz plane) of the density ρ . Fig. 9 shows $\Delta\rho$ in the central part of the PNS remnant (as it is the main responsible for the GW emission). The nonrotating progenitor can be very well approximated by a spherically symmetric mass distribution, even for $t > t_b$. In fact, the density fluctuations in the `nrot` model are at least one order of magnitude smaller than in the models with rotating progenitors, therefore GW signals will be enhanced for the rotating models. Another effect due to rotation is the thick disk on the equatorial plane. For the rotating cases, in the equatorial plane, we can see that at early times there is a noticeable quadrupolar mass distribution, followed by a somewhat longer lasting dipolar distribution.

A more quantitative description of the results shown in Fig. 9 is obtained by the mode decomposition of the density in the equatorial plane. The mode coefficients ρ_m are defined as

$$\rho_m \equiv \int \sqrt{\gamma} \rho W e^{-im\phi} dx dy, \quad (3)$$

where W is the Lorentz factor, γ is the 3-metric determinant and $\rho dx dy$ is the surface density in the equatorial plane. These results are shown in Fig. 10. In the nonrotating case, all modes have relative amplitude (ρ_m/ρ_0) below 2×10^{-3} for all times. The cases with non-zero initial spin exhibit a prominent peak of the $m = 2$ mode at approximately 40 milliseconds after the bounce. For both rotating cases, the $m = 2$ mode decays rapidly after the peak, after which the $m = 1$ mode becomes the dominant mode. While all other modes tend to decay after 80 ms, the $m = 1$ mode lingers on. This $m = 1$ feature is related to the one-armed instability (Ott et al. 2005; Ou & Tohline 2006; Kashyap et al. 2017).

The gravitational waveforms of our three models are presented in Fig. 11. The GW signals were obtained with two different methods. In the first one, we perform a fixed-frequency double time integration of the Weyl scalar ψ_4 for all $l = 2$ modes. In this method, we use a high-pass filter to keep only frequencies higher than 120 Hz, in order to mitigate the numerical noise at lower frequencies. The second method for obtaining the GW emission used the quadrupole formula (Maggiore 2007), where no post-processing noise mitigation was employed. The resulting GWs from both methods are shown in Fig. 11. Although there is good qualitative agreement between the two ways of reconstructing the waveform, there are clear quantitative disagreements between them, specially in the `nrot` case, due to the different treatment of numerical noise in each method. Consistent with this interpretation, the `nrot` model is more affected as its low GW amplitude is comparable to the numerical noise found in our numerical evolution. One should also have in mind that while the quadrupole formula is approximate (low velocity, weak gravity, and long GW wavelength approximations), while ψ_4 is exact, but potentially more sensitive to numerical noise.

As expected, Fig. 11 shows that rotating progenitors should emit GWs with higher amplitudes. The nonrotating `nrot` model yields a GW signal with similar amplitude to a CCSNe with a nonrotating progenitor (Powell & Müller 2022; Yakunin et al. 2015; Kuroda et al. 2017; Dolence et al. 2015; Murphy et al. 2009; Müller et al. 2013; Marek et al. 2009; Mezzacappa et al. 2022; Nakamura et al. 2022; Morozova et al. 2018; David Radice & et al. 2019; Mezzacappa et al. 2023; Vartanyan et al. 2023). The perturbations of the PNS perturbation are amplified by the initial angular momentum (see Figs. 9 and 10), strengthening the GW signals. Comparing our models, we see that the `rot` model radiates a strain that is up to two orders of

Model	LIGO	CE	ET
<code>nrot</code> (Ψ_4 edge-on)	1.7×10^1	1.5×10^2	7.7×10^1
<code>nrot</code> (Quad. edge-on)	1.1×10^1	7.7×10^1	5.5×10^1
<code>nrot</code> (Ψ_4 face-on)	2.1×10^0	1.8×10^1	9.5×10^0
<code>nrot</code> (Quad. face-on)	6.7×10^0	4.9×10^1	3.4×10^1
<code>rot_ar075</code> (Ψ_4 edge-on)	4.3×10^2	3.7×10^3	1.9×10^3
<code>rot_ar075</code> (Quad. edge-on)	4.3×10^2	3.6×10^3	2.0×10^3
<code>rot_ar075</code> (Ψ_4 face-on)	7.8×10^2	6.7×10^3	3.5×10^3
<code>rot_ar075</code> (Quad. face-on)	8.1×10^2	6.9×10^3	3.7×10^3
<code>rot</code> (Ψ_4 edge-on)	5.1×10^2	4.4×10^3	2.3×10^3
<code>rot</code> (Quad. edge-on)	5.1×10^2	4.3×10^3	2.3×10^3
<code>rot</code> (Ψ_4 face-on)	9.5×10^2	8.2×10^3	4.3×10^3
<code>rot</code> (Quad. face-on)	9.7×10^2	8.3×10^3	4.4×10^3

Table 2. Signal to noise ratio (SNR) of our models for different WG detectors: advanced LIGO, Cosmic Explorer (CE), and Einstein Telescope (ET). All SNRs shown in this table were calculated for the full $l = 2$ mode at 10kpc, see Fig. 14. We show values obtained both by using the quadrupole approximation and performing strain reconstruction via Ψ_4 . The discrepancies in SNR obtained through different methods can be understood by the fact that they have very distinct noise mitigation schemes. Therefore the final strain obtained in each method is subjected to different levels of noise. In particular, the `nrot` model is more affected by these uncertainties as its strain amplitude is comparable to the numerical noise present in our simulations, see Fig. 11.

magnitude stronger than the `nrot` model. Our `rot_ar075` and `rot` models have initial angular velocities of 5.09 Hz and 5.28 Hz, emit GWs with amplitudes between $Dh \sim 200$ cm and $Dh \sim 600$ cm and exhibit a peak frequency of ~ 1000 Hz. As AICs are expect to rotate faster than CCSNe, we argue that AICs are more likely to produce loud high-frequency signals than CCSNe. Shibagaki et al. (2020) and Shibagaki et al. (2021) studied the GW signal emitted by CCSNe with rotating progenitors ($1 \text{ Hz} < \Omega < 2 \text{ Hz}$). In their analysis they found that these events display a GW strain amplitude between $Dh \sim 60$ cm and $Dh \sim 300$ cm, with peak frequency varying from ~ 400 to ~ 900 Hz. The amplitudes and frequencies of these signals increase systematically with rotation.

Our rotating models exhibit a prominent $m = 0$ pulse early in the post-bounce phase, identified by the modal decomposition of Ψ_4 (not shown here). The fact that the initial $m = 0$ GW mode disappears in the face-on inclination is a reflection of the different weights, coming from the spin-weighted spherical harmonics basis that each mode has for a given observation angle. This early $m = 0$ GW emission is consistent with results from the 2D simulations of Abdikamalov et al. (2010).

As Abdikamalov et al. (2010) were limited to 2D simulations, they could only access the $l = 2$, $m = 0$ mode. Here we moved to 3D models, allowing us to look into higher modes. Given that the quadrupolar contribution is expected to be dominant, we focused our study on the full $l = 2$ mode. After the prompt (lower frequency) GW emission close to $t - t_b = 0$, we see a higher frequency signal starting ≈ 20 ms after the bounce and lasting up to $t - t_b \approx 80$ ms, as can be seen in Fig. 11. The initial low-frequency signal is produced by the bounce of the PNS core, whereas the later high-frequency emission is related to the highly perturbed PNS. The asymmetry in the matter distribution of the PNS grows in amplitude until it generates a GW signal comparable to the prompt emission (see Figs. 9 and 10).

Hayama et al. (2018) showed that the polarization of the GWs of a CCSN can carry information about the EOS of the remnant PNS. The standing accretion shock instability (SASI), present or absent depending on EOS, produces GWs that are circularly polarized, but the sign of the polarization can change abruptly during the CCSN evolution. In contrast to this polarized signal, the GWs emitted by

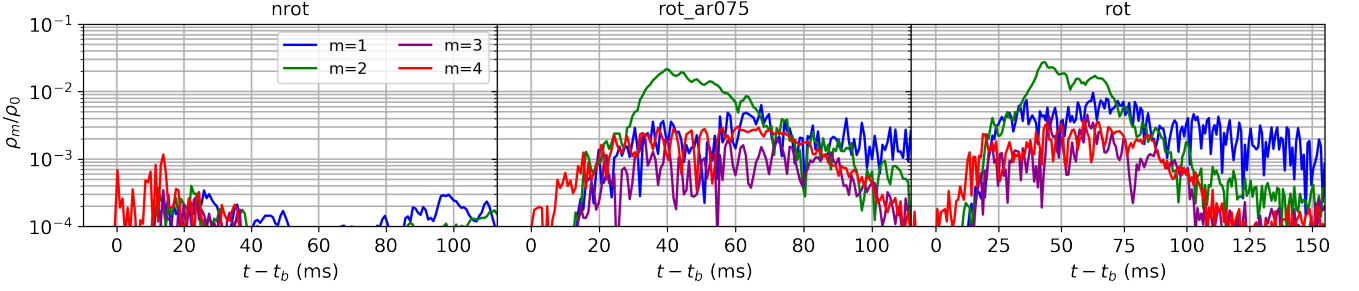


Figure 10. Mode decomposition of the density in the equatorial plane, see Equation (3). The **nrot** model maintains an approximately spherical mass distribution, as all modes have relative amplitude lower than 0.1% at all times. For the models with rotating progenitors, the $m = 2$ mode is dominant from ≈ 20 ms to ≈ 80 ms after the bounce, peaking at a relative amplitude of 2-3%. At later times $t - t_b \gtrsim 80$ ms, the $m = 1$ mode becomes dominant, maintaining a relative amplitude approximately 10 times higher than the other modes.

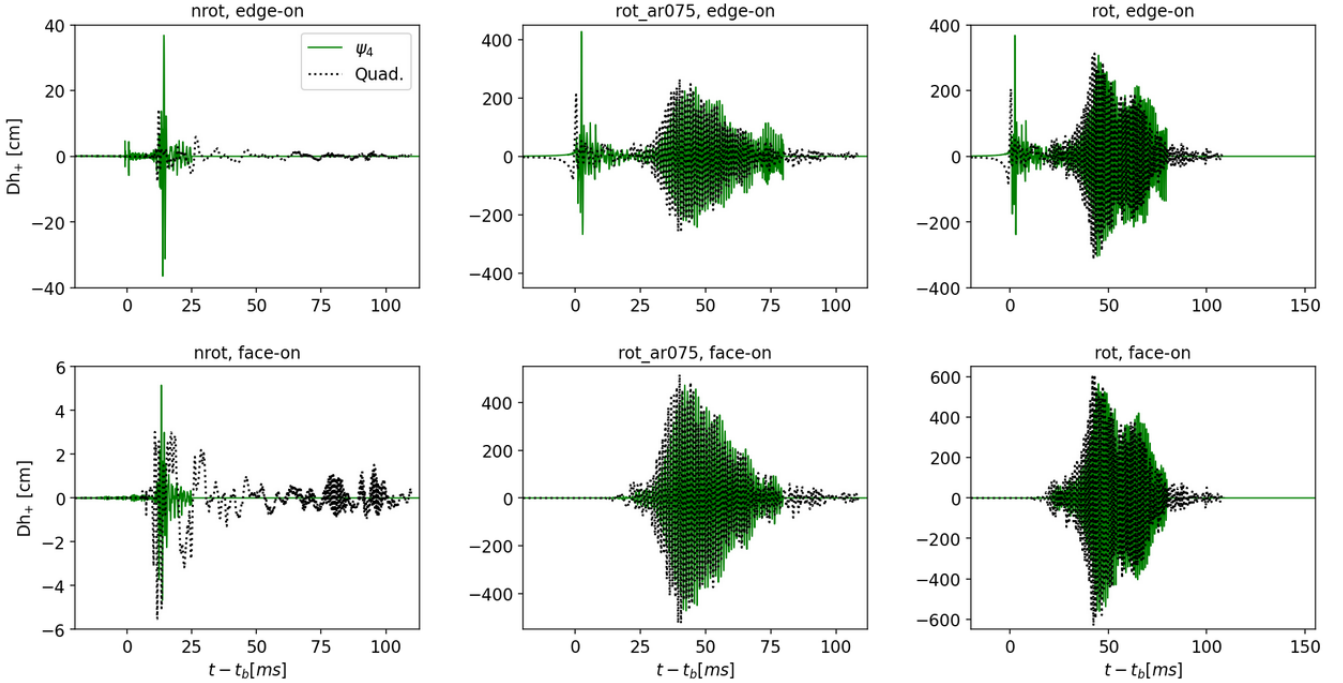


Figure 11. GW emission in the time domain. Here we compare the GW strain ($l = 2$ mode) obtained via the quadrupole approximation and with the waveform reconstruction from Ψ_4 . In the edge-on configuration, we can see a prompt $m = 0$ signal, followed by a very loud $|m| > 0$ pulse coincident with the ρ_2 perturbation shown in Fig. 10. (We are able to identify the $m = 0$ contribution based on an analysis of Ψ_4 , which is originally obtained in the spin-weighted spherical harmonics basis. The signal shown here represents the full $l = 2$ mode.) Note that some features vanish when moving from the edge-on to the face-on orientation. This is due the different angular dependence of each one of the m modes. The prompt emission is morphologically consistent with the results from Abdikamalov et al. (2010). The overall amplitude of the GWs emitted by our non-rotating model is consistent with simulations of GWs from nonrotating CCSNe (David Radice & et 2019). On the other hand, initial angular momentum seems to amplify the signals by up to two orders of magnitude.

the fundamental mode of oscillation of the PNS in their models are randomly polarized. This separation can be clearly seen in Fig. 1 of Hayama et al. (2018). In Fig. 12 we show the polarization plots for our models, obtained with the quadrupole formula. In our rotating models, we find that the $l = 2$ polarization is circular with no sign change in the face-on configuration. The observed polarization is more complex in the edge-on case, due to the presence of the linearly polarized $m = 0$ mode at early times, see Fig. 13.

In order to assess the detectability of GWs emitted by AIC events, we plot in Fig. 14 our simulated signals at a fiducial distance of 10 kpc together with the sensitivity curves of LIGO and future GW detectors Cosmic Explorer (CE; Abbott et al. 2017) and Einstein Telescope (ET; Punturo et al. 2010). All noise curves were retrieved

from Borhanian (2021). We define the signal to noise ratio (SNR) as

$$\left(\frac{S}{N}\right) \equiv \int_0^\infty df \frac{|\tilde{h}(f)|^2}{S_n(f)}, \quad (4)$$

where $\tilde{h}(f)$ and $S_n(f)$ are respectively the GW strain in the frequency domain and the single-sided noise spectral density. If we require a single-detector SNR of 8 for detectability, then the GW detection horizon for the most optimistic scenario, i.e. a maximally rotating AIC observed face-on, ranges from ~ 1.2 Mpc (for LIGO) to ~ 10 Mpc (for a 40 km CE). The **nrot** model would only be detectable

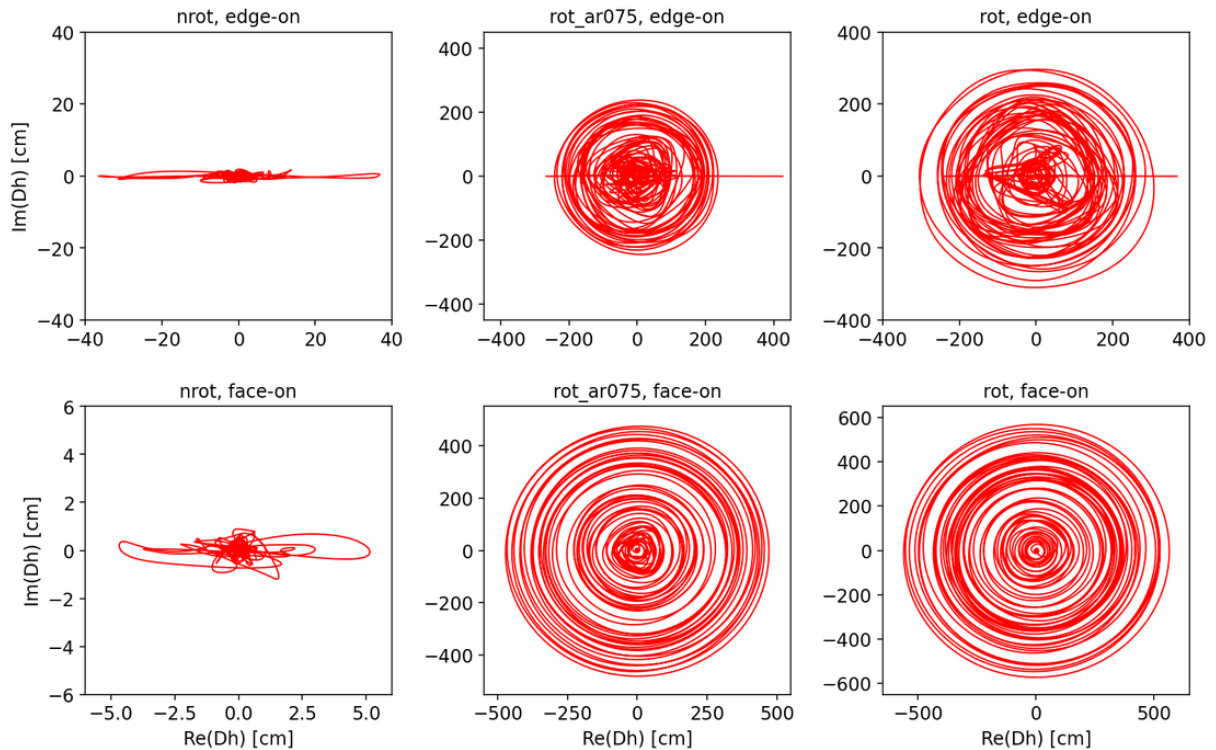


Figure 12. GW polarization patterns using the strain calculated via the Weyl scalar Ψ_4 . For the face-on configuration, the signal follows a very clear circular polarization. The polarization is more complex for the edge-on case, due to the prompt $m = 0$ mode which holds a linear polarization. The nrot model is mostly linear polarized but is notably affected by numerical errors.

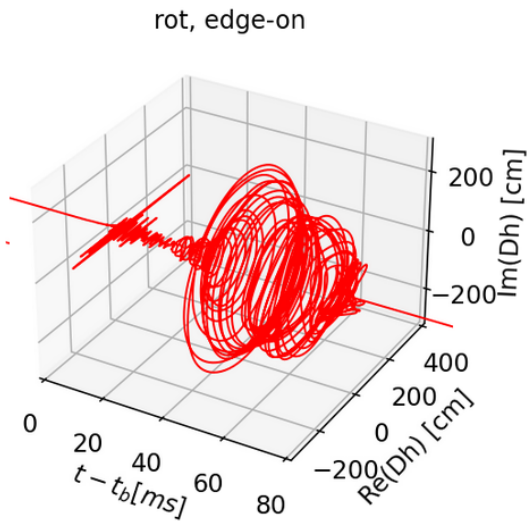


Figure 13. Temporal evolution of the GW polarization pattern for rot in the edge-on alignment. Note that at early times the signal displays a linear polarization associated with the prompt $m = 0$ GW emission. The circular polarization corresponds to the $m = 2$ GW mode. The strain used is the one obtained via the Weyl scalar Ψ_4 .

by CE with SNR = 8 at a maximum distance of ≈ 19 kpc. See Table 2 for more details.

The rate of AICs in the galaxy is still very uncertain. In order to estimate the AIC detection rate by future GW detectors, we assume the AIC rate to be of the order of 10% of the SNIa rate, which is esti-

mated as approximately $3 \times 10^{-4} \text{ yr}^{-1} \text{ Mpc}^{-3}$ (Cappellaro et al. 2015). Our detection horizons for a maximally rotating AIC (best case scenario), yield detection rates of approximately $(x/10\%) \times 0.14 \text{ yr}^{-1}$ (for CE) and $(x/10\%) \times 2.2 \times 10^{-4} \text{ yr}^{-1}$ (for LIGO), where x is the (still highly uncertain) true ratio between AIC and SNIa event rates in percentage form.

Our estimated rates are consistent with those made by Fryer et al. (1999) using nucleosynthesis arguments, which imply an upper limit of 0.08 yr^{-1} within our estimated GW detection horizon for CE. This upper limit, obtained by attributing the formation of all r -process elements to AICs, may need to be revised after more 3D simulations become available. For example, our simulations show that the ejecta material has higher Y_e than reported by Fryer et al. (1999), which would push their reported upper limits for the AIC rates to higher values.

The numbers in Table 2 implicitly assume that the signals were identified through a match-filtering search with a large waveform template bank for these events. In reality, the first detection of an AIC will likely be achieved by a burst analysis (Klimenko et al. 2021), which is less sensitive than a match-filtering search. In this case, we can expect a decrease by a factor of order unity in the detection horizon (Mohapatra et al. 2014), nevertheless, the resulting CE observation volume would still include (at least) the Local Group of galaxies representing an improvement compared to LIGO.

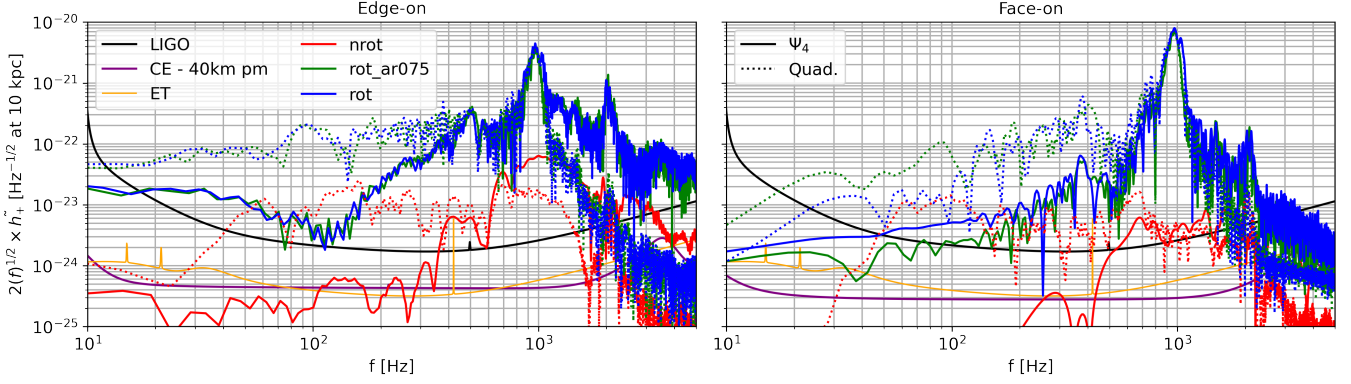
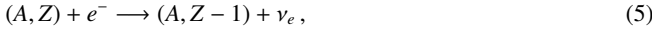


Figure 14. Amplitude spectral density for our models. Here we compare the strain ($l = 2$ mode) as obtained via the quadrupole approximation and the waveform reconstruction from Ψ_4 . We show the result for the cases of face-on and edge-on orientation of the source. We compare the signal with the design sensitivity of LIGO, a post-merger (pm) optimized 40 km CE, and ET. The associated SNR for each case is shown in Table 2. Comparing our results to those of CCSNe, we see that the overall amplitude of our non-rotating model is similar to non-rotating CCSNe. On the other hand, initial angular momentum seems to amplify the signals by two orders of magnitude.

5 NEUTRINO EMISSION

5.1 Electron capture

During the collapse, the increasing density drives up the electron Fermi energy and consequently leads to electron capture inside the WD:



where (A, Z) is a nucleus of atomic number Z and atomic mass A . In our simulations, the nucleon number densities are computed via the prescription for $Y_e(\rho)$ described by Liebendörfer (2005) and no neutrino emission is included for $t < t_b$. After the bounce, we treat neutrinos using the M1 grey scheme of Radice et al. (2022). It is useful to define the chemical potential imbalance (Hammond et al. 2021) as

$$\mu_\delta \equiv \mu_n + \mu_{\nu_e} - \mu_p - \mu_e \quad (6)$$

where μ_n , μ_p , μ_e , and μ_{ν_e} are the chemical potentials of neutrons, protons, electrons, and neutrinos, respectively. The neutrino chemical potential is implicitly defined by

$$Y_{\nu_i} \equiv \frac{n_{\nu_i}}{n_p + n_n} = \frac{4\pi m_b}{\rho (hc)^3} (k_B T)^3 F_2 \left(\frac{\mu_{\nu_e}}{k_B T} \right), \quad (7)$$

where Y_{ν_i} , n_{ν_i} , T , and m_b are the neutrino fraction and the neutrino number density, the temperature, and the baryon effective mass, respectively, and F_2 is the Fermi integral of the second order, which can be obtained for cases of physical interest by

$$F_k(x) \equiv \int_0^\infty \frac{y^k dy}{e^{y-x} + 1} = -\Gamma(1+k) \text{Li}_{k+1}(-e^x), \quad \text{Re}(k) > -1, \quad (8)$$

where Li_k is the polylogarithm function of the k -th order (Perego et al. 2019). The chemical potential imbalance in our models can be seen in Fig. 15. Comparing Fig. 15 and Fig. 5, we can see that the infalling material has $\mu_\delta < 0$. This implies that the electron capture process is preferred over neutrino absorption. On the other hand, the central part of the star has $\mu_\delta \approx 0$, implying a weak equilibrium of the fluid.

5.2 Neutrino emission

The temporal evolution of the ν_e energy flux (F_{ν_e}) is depicted in Fig. 16. For $r \geq 40$ km F_{ν_e} has a visible outgoing radial component that becomes more dominant at larger distances from the center of the star. In the last snapshot of Fig. 16 (bottom panel), it is possible to see a blue surface around the core of the remnant PNS. This surface separates the exterior region where the radial component of the energy flux is positive (outgoing) from the interior region presenting an energy flux with an overall negative (ingoing) radial component, as indicated by the direction of the arrows. The existence of a central region from which the neutrinos are not escaping implies the existence of trapped neutrinos. In practice, this means that the intense flux in the center will not be released immediately. It will take some time ($O(1$ min); Roberts & Reddy 2017) for the PNS to cool down in order to become transparent to these neutrinos.

Similar to the bottom panel of Fig. 16, Fig. 17 depicts the neutrino energy flux in the central part of the remnant PNS for different neutrino flavors. In this figure, we insert black lines (fixed at the surface of zero radial energy flux of ν_e in the rot model) to aid a visual size comparison between the different models. From this figure, we can see that the different neutrino flavors start to stream outwards at different radii. The surface of zero radial energy flux is largest for ν_e , followed by $\bar{\nu}_e$, and ν_x . As we argue in the next few paragraphs, the surface of zero radial energy flux is related to the surface of thermal decoupling, and its location leaves imprints on the average neutrino energy.

To compute the neutrino fluxes as seen by a distant observer, we performed the surface integral of the proper flux defined as $\mathcal{F}_\nu^i \equiv \sqrt{\gamma} (\alpha F_\nu^i - \beta^i E_\nu)$, where F_ν^i and E_ν are the neutrino flux and energy in the Eulerian frame, α is the lapse function and β^i is the shift vector. Accordingly, the neutrino luminosity is given by

$$L_\nu = \int_{S_r} \hat{r}_i \mathcal{F}_\nu^i dS, \quad (9)$$

where \hat{r}_i is the unit covector normal to a coordinate sphere S of radius r . The neutrino luminosities we obtain in our simulations are summarized in Fig. 18. There is a large peak in the luminosity near the time of bounce, which is present in all neutrino flavors for our three models. The total luminosity of each neutrino flavor varies over time from $\sim 10^{51}$ to $\sim 10^{54}$ erg/s. At early times $t - t_b \lesssim 20$ ms, we have

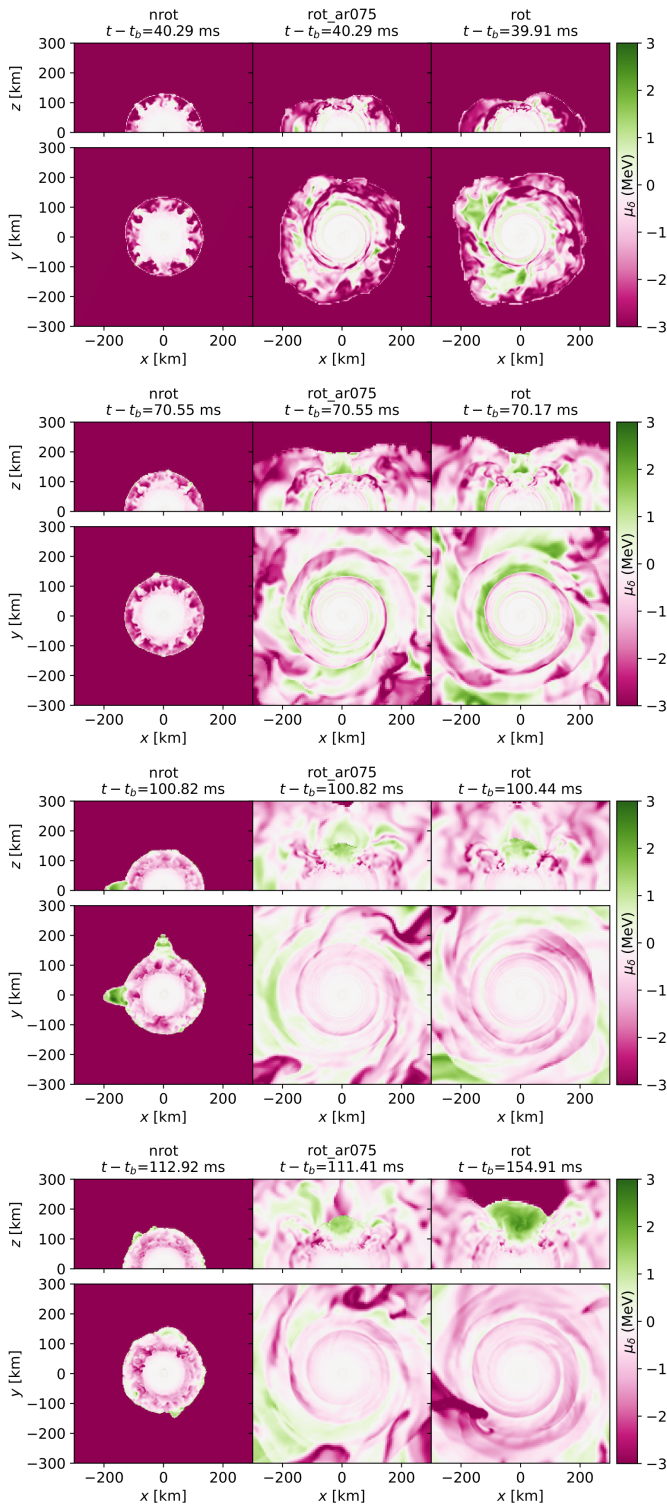


Figure 15. Chemical potential imbalance, defined in eq. (6), for the inverse β -decay process. Negative values indicate a tendency to neutronize the material, by emitting neutrinos via inverse β -decay, see eq. (5). The polar regions with positive μ_δ are more affected by the neutrino wind and can be related to the high entropy bubble being ejected near the pole (see Fig. 6)

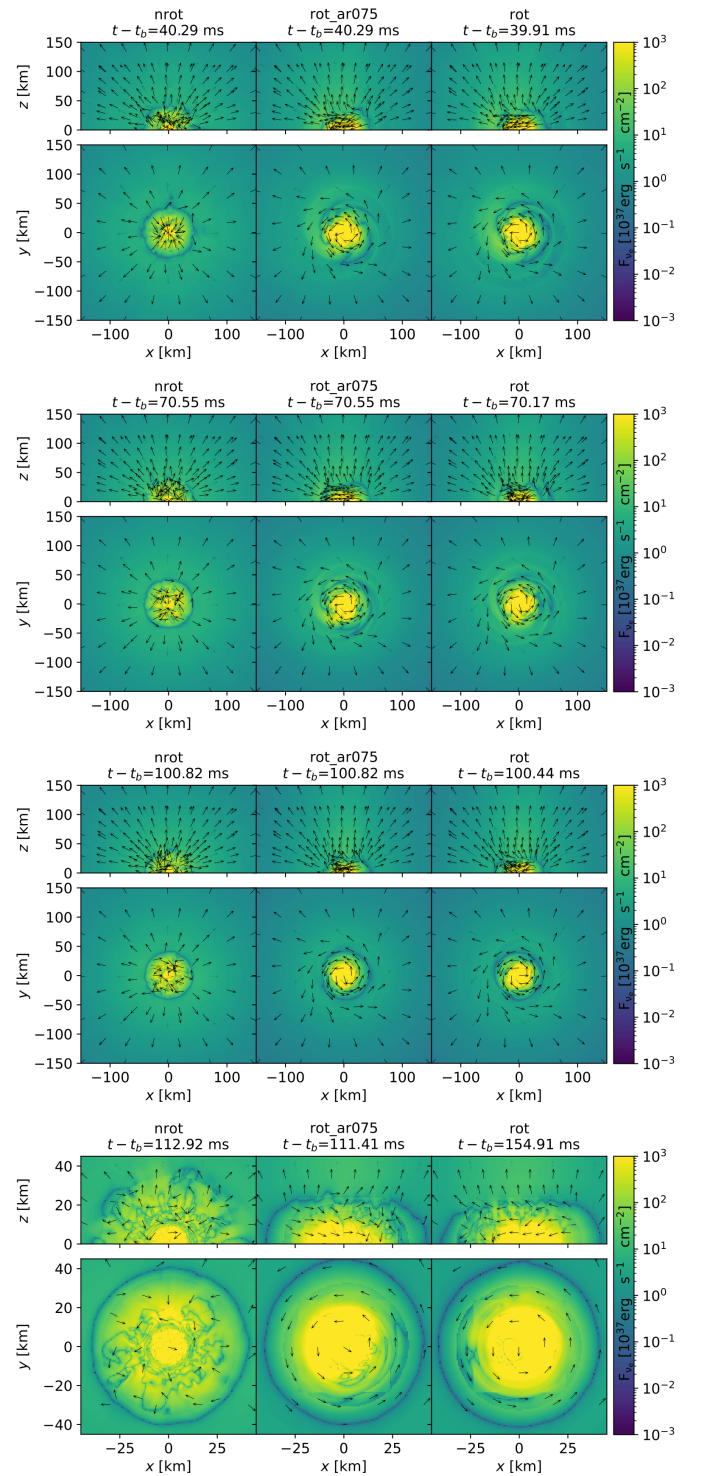


Figure 16. Energy flux of ν_e . The color scheme represents the intensity of the radial flux component. Arrows represent the local direction of the energy flux. The bottom panel is zoomed-in to show smaller scale details: there is a clear radially outgoing flux at large radii, but not in the core. This fact can be seen more easily in the xy (yz) plane for nrot (rot_ar075 and rot). The surface of zero radial energy flux appears as a blue ring in the equatorial plane and it is related to the surface of thermal decoupling. Note the effect of rotation on this surface: it appears at larger radii for the rotating progenitors. The emission becomes more axisymmetric with rotation.

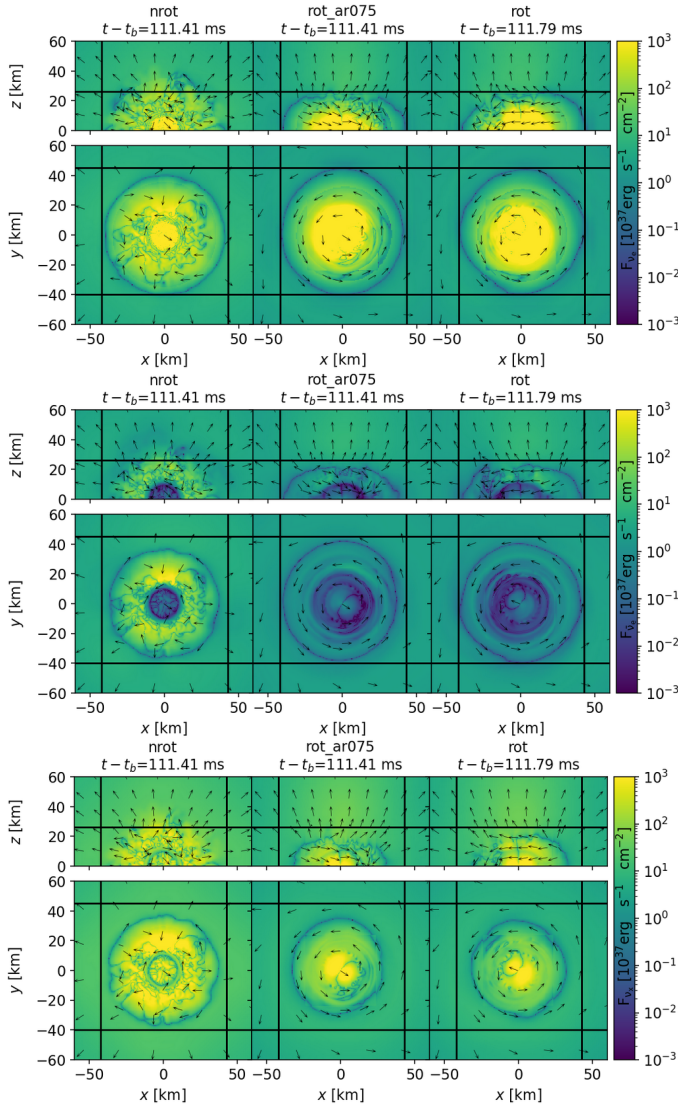


Figure 17. Energy flux of neutrinos (from top to bottom: ν_e , $\bar{\nu}_e$, and ν_x representing heavy lepton neutrinos), similar to the bottom panel of Fig. 16. The black lines represent the size of the zero radial energy flux for ν_e in the rot model, and are included to facilitate a visual size comparison between different neutrino flavors and models. The radius of the surface of zero radial energy flux is different for each neutrino flavor (neutrinos can stream outwards freely when outside the largest surface with zero flux, if more than one is present, as in the $\bar{\nu}_e$ case). This has a visible imprint in the average neutrino energy, see Fig. 20. As the inner core of the star is hotter, neutrinos emitted from more central regions will be more energetic.

$L_{\bar{\nu}_e} < L_{\nu_x} < L_{\nu_e}$, but at later times the electron neutrino luminosity drops below the heavy lepton neutrino luminosity, while the electron antineutrino emission remains subdominant, i.e. $L_{\bar{\nu}_e} < L_{\nu_e} < L_{\nu_x}$. This sharp decrease in L_{ν_e} is related to the behavior of Y_e after the bounce. Although not shown in Fig. 2, during the collapse phase we have $Y_e \gtrsim 0.3$. Shortly after the bounce ($t - t_b \approx 7$ ms) the PNS reaches $Y_e \lesssim 0.2$ for the first time in a thin ring (in the xy plane) that expands for the next tens of ms. The further decrease in Y_e naturally suppresses the inverse β -decay as there will be less electrons available to be captured. After $t - t_b \approx 20$ ms, the low- Y_e ($\lesssim 0.2$) region remains within a radius of $r \approx 100$ km and Y_e evolves more slowly, consistently with the slow evolution of L_{ν_e} at late times. Increasing the rotation of the WD progenitor suppresses

the ν -emission of all flavors because the centrifugal forces pushes the material to larger radii resulting in lower temperatures, see Fig. 19.

Another observable of interest for the neutrino emission process is the average neutrino energy $\langle E_\nu/N_\nu \rangle$, shown in Fig. 20. Although the electron neutrinos have the highest luminosity, they have the lowest average energy because they also have the highest number density. The average neutrino energy is related to the temperature of the surface of the thermal decoupling of each neutrino type. Heavy-lepton neutrinos are the most energetic and become thermally decoupled in innermost regions of the PNS, whereas electron neutrinos are the least energetic and decouple further away from the PNS center, as can be seen by comparing the temperature maps shown in Fig. 19 and the surfaces of zero radial flux in Fig. 17.

Our neutrino luminosity and average neutrino energy are in good qualitative and quantitative agreement with those reported in the CCSN literature (Nagakura et al. 2020; Warren et al. 2020; Burrows et al. 2019; Müller & Janka 2014; Müller et al. 2017). Our results agree quantitatively with these earlier papers, where the neutrino luminosities and average neutrino energies for all flavors were found to be between $\sim 2 - 8 \times 10^{52}$ erg/s and $\sim 9 - 16$ MeV, respectively, for similar times scales as those considered here. As in the case for the neutrino luminosities, the addition of angular momentum suppresses the average neutrino energy irrespective of their flavors.

6 EJECTA AND ELECTROMAGNETIC COUNTERPART

In order to estimate the ejecta mass we use the Bernoulli criterion (Kastaun & Galeazzi 2015; Haddadi et al. 2023), according to which fluid elements are unbound if they satisfy

$$hu_t \leq -h_{min}, \quad (10)$$

where h is the enthalpy, u_t is the time component of the fluid 4-velocity and h_{min} is the minimum enthalpy value allowed by our EOS table. The Bernoulli criterion assumes that the fluid is in a steady-state configuration, but our models are highly dynamic. Thus Equation 10 should be used only as an approximation/upper limit: the amount of ejecta can be overestimated because this criterion assumes that the internal energy of the fluid is completely transformed into kinetic energy. We also require that fluid elements satisfying the Bernoulli criterion should move outward ($v^r > 0$) in order to be considered unbound. Finally, we only analyze material inside a radius of 1200 km, in order to avoid any contamination from spurious outflow material on the edge of the star. The shock front did not exceed this radius during our simulations.

The first quantity of interest for the ejecta is the diagnostic explosion energy, presented in Fig. 21. We calculate the diagnostic explosion energy as:

$$E_{\text{exp}} = \int_V (\rho \varepsilon W^2 + \rho W(W-1) + P(W^2-1)) \sqrt{\gamma} dV, \quad (11)$$

where the first term represents the internal energy of the fluid (ε is the specific internal energy), the second term is the kinetic energy and the last term accounts for the pressure (P) contribution. The volume V , over which the integral in Equation (11) is evaluated, is the volume occupied by outgoing fluid elements satisfying the Bernoulli criterion, given by Equation (10). We note that the diagnostic explosion energy overestimates how much internal energy is transformed into kinetic energy during the explosion, in addition to using the overestimated ejecta amount based on the Bernoulli criterion.

The diagnostic explosion energy for the nrot model is found to

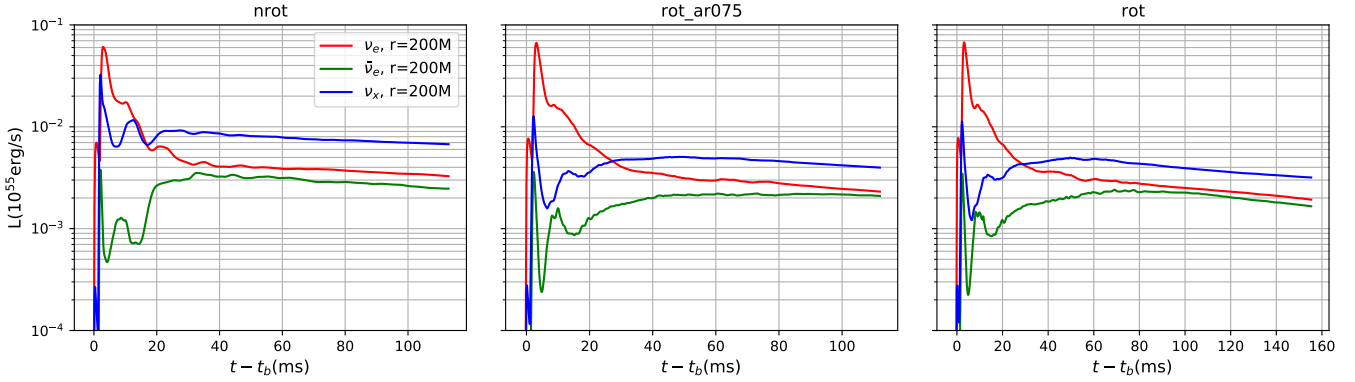


Figure 18. Neutrinos luminosities. Electron neutrinos show an intense prompt emission followed by a sharp decay. Heavy lepton neutrinos dominate the late-time emission. Models with rotating progenitors have lower neutrino emission, see also Fig. 20.

be numerically consistent with zero. For the two rotating models, the diagnostic explosion energies are approximately 5×10^{50} and 6×10^{50} ergs for the *rot_ar075* and *rot* models, respectively. Rotation seems to favor mass ejection: *nrot* does not present any ejecta, whereas both *rot_ar075* and *rot* eject $M_{\text{ej}} \approx 3 \times 10^{-2} M_{\odot}$, in good agreement with the “naked AIC” model proposed by Metzger et al. (2009a). From explosion energies and ejecta masses we can estimate the asymptotic velocities at radial infinity as $v_{\infty}^r \approx (2E_{\text{exp}}/M_{\text{ej}})^{1/2} \approx 0.14c$ for both *rot_ar075* and *rot*.

The properties of the ejecta are presented in Fig. 22, which displays the temperature, electron fraction, entropy and radial velocity as a function of density. Notably, the radial velocities observed in the ejecta are only a fraction of those obtained from the explosion energy estimates. However, this apparent contradiction can be reconciled by understanding that Fig. 22 represents only a snapshot of the time evolution of the system. Therefore, the velocities observed in the plot are not yet the asymptotic values.

Furthermore, lower density material in the ejecta shows higher velocities. At the same time, the electron fraction distribution ranges from ≈ 0.1 to ≈ 0.5 . We estimate $Y_e \approx 0.46$ for the lowest density ejecta material ($\rho \leq 10^8 \text{ g/cm}^3$), using a mass-weighted average. Therefore, it is essential to consider the time evolution of the system and the behavior of low-density material to draw accurate conclusions about the properties of the ejecta.

We estimate the peak luminosity of the light curve following Arnett (1980) and Metzger (2019)

$$L_{\text{peak}} \approx 10^{41} \text{ erg s}^{-1} \left(\frac{M_{\text{ej}}}{10^{-2} M_{\odot}} \right)^{0.35} \left(\frac{v}{0.1c} \frac{1 \text{ cm}^2 \text{ g}^{-1}}{\kappa} \right)^{0.65} \quad (12)$$

and time of peak luminosity t_{peak} is estimated as

$$t_{\text{peak}} \approx 1.6 \text{ days} \left(\frac{M_{\text{ej}}}{10^{-2} M_{\odot}} \right)^{1/2} \left(\frac{v}{0.1c} \frac{1 \text{ cm}^2 \text{ g}^{-1}}{\kappa} \right)^{-1/2}, \quad (13)$$

where κ is the fluid opacity, v is the ejecta material typical velocity, and M_{ej} is the total ejecta mass. Our analysis reveals that the ejecta mass has a nearly symmetric composition. To approximate the opacity of the ejecta material, we follow Kasen et al. (2013) and assume it to be composed by elements of the iron group (a mixture of 10% Ni, 80% Co, 10% Fe), which has a wavelength-dependent opacity ranging from $\sim 0.6 \text{ cm}^2/\text{g}$ to $\sim 0.01 \text{ cm}^2/\text{g}$ in the optical band (4000 \AA to 10000 \AA). For our analysis, we use a representative value $\kappa = 0.2 \text{ cm}^2/\text{g}$. By applying Arnett’s law (Equations 12 and 13), we obtain estimates for L_{peak} and t_{peak} : $\sim 5.1 \times 10^{41} \text{ erg/s}$ and 1 day for

the *rot_ar075* model, and $\sim 5.5 \times 10^{41} \text{ erg/s}$ and 1.3 days for the *rot* models, similar to the predictions for the “naked AIC” model presented in (Metzger et al. 2009a).

Our estimates for the peak luminosity of our AIC models are 2 orders of magnitude lower than for CCSNe and SNIa, see for example Khokhlov et al. (1993); Arnett (1996); Woosley et al. (2007); Morozova et al. (2020). This difference is largely influenced by the fact that our models predict very low mass ejecta compared to CCSNe and SNIa. Also, the evolution timescale of the AIC light curves (less than two days for our models) is about a tenth of the timescale for CCSNe and SNIa (typically a few weeks). These differences are a consequence of the low ejecta mass and rapid rotation achieved in our models.

7 CONCLUSIONS AND FUTURE WORK

Accretion-induced collapse (AIC) of WDs is a theorized possible source for multimessenger astronomy and, in particular, of GWs for next-generation ground-based detectors. We perform numerical simulations of three AIC models, starting with WD progenitors that are nonrotating, fast rotating or maximally rotating. Our main results are as follows:

(i) The non-rotating progenitor leads to a fairly spherical symmetric AIC, with no spiral arms forming as the shock seems to stall. Our rotating progenitors form spiral arms and a thick disk on the equatorial plane surrounding the PNS remnant. Rotation also induces the excitation of higher order modes in the mass distribution. A transient $m = 2$ mode is connected to the GW emission; a long-lived $m = 1$ mode with approximately constant amplitude may be related to the one-armed instability (Abdikamalov et al. 2010).

(ii) GW radiation of AICs is strongly enhanced in our models with rotating progenitors, with amplitudes 1-2 orders of magnitude stronger than predictions for CCSNe with slowly rotating progenitors. CCSNe with fast-rotating ($\Omega = 2 \text{ Hz}$) progenitors display GW signals similar to our models with rotation although still $\sim 30\%$ fainter and with $\sim 10\%$ lower frequencies. Our results imply that the additional rotational energy is the decisive feature for the stronger GW emission of AICs when compared to CCSNe. The AIC detection horizon (for the maximally rotating model in a face-on configuration) is approximately 10 Mpc for CE and 1.2 Mpc for LIGO. Estimated detection rates are $(x/10\%) \times 0.14 \text{ yr}^{-1}$ for CE and $(x/10\%) \times 2.2 \times 10^{-4} \text{ yr}^{-1}$ for LIGO, where x is the ratio (in percentage form) between AIC and SNIa event rates.

(iii) Neutrino emission from all of our AIC models is comparable with that of CCSNe.

(iv) Electromagnetic emission of our rotating AIC models is estimated to be approximately 5×10^{41} erg/s, i.e. two orders of magnitude dimmer than SNIa models (Khokhlov et al. 1993; Arnett 1996; Woosley et al. 2007; Morozova et al. 2020), with peak times between one and two days. Our predictions are in agreement with the previous estimates of Metzger et al. (2009b) and Darbha et al. (2010), although their mass ejection mechanism is different from the one considered here. At the distances accessible to GW detectors, however, this would be a very bright transient.

The estimated light curve properties of AICs indicate that an AIC detection based on their optical transient alone (without a GW counterpart) would be rather challenging. WD ZTF J190132.9+145808.7 (Caiazza et al. 2021) is a possible candidate for a future AIC progenitor. This object is very close to the Chandrasekhar mass limit ($M \approx 1.327 - 1.365 M_{\odot}$) with a rotation period of 6.94 minutes and seems to be cooling down via electron capture on sodium.

As usual, the inclusion of magnetic fields would be desirable for a better description of these astrophysical events. Because AIC progenitors are expected to be rapidly rotating due to their accretion history, existing magnetic fields are expected to be amplified during the collapse but details are still uncertain. Yi & Blackman (1998), Metzger et al. (2008), and Perley et al. (2009) suggested that AICs could power GRBs; we see that some conditions for the formation of jets are already present in our simulations, but conclusions regarding jet formation should wait until the full inclusion of magnetic fields in the simulation. We are currently studying the implementation of magnetic field effects via the general-relativistic magnetohydrodynamical Gmnu code (Cheong et al. 2020, 2021, 2022), which recently has been updated in order to include a two-moment based multi-frequency neutrino radiation scheme (Cheong et al. 2023). Including magnetic fields will allow us to assess effects such as jet formation and evolution of the light curves. These two effects are essential for comparing our AIC models with a GRB event such as GRB211211A (Rastinejad et al. 2022). It will also be interesting to investigate whether the oscillations of a PNS formed in an AIC could explain the pulsations observed in some short GRB light curves (Chirenti et al. 2023). Relaxing the assumption of the deleptonization scheme by Liebendörfer (2005) and including possible environmental effects (such as a remaining accretion disk) also constitute an interesting avenue of investigation.

ACKNOWLEDGEMENTS

It is a pleasure to acknowledge Viktoriya Morozova for performing the collapse portion of the simulations and Ernazar Abdikamalov for providing the deleptonization table. We are grateful to Brian Metzger for his input on a previous version of this manuscript. LFLM also acknowledges useful discussions with Cole Miller, Igor Andreoni, John Baker, and Scott Noble. LFLM thanks the financial support of the São Paulo Research Foundation (FAPESP) grant 2021/09531-5 under the BEPE program, and thanks Pennsylvania State University for the hospitality during the realization of this project. DR acknowledges funding from the U.S. Department of Energy, Office of Science, Division of Nuclear Physics under Award Number(s) DE-SC0021177 and from the National Science Foundation under Grants No. PHY-2011725, PHY-2020275, PHY-2116686, and AST-2108467. CC acknowledges support by NASA under award numbers 80GSFC17M0002 and TCAN80NSSC18K1488,

and of the Aspen Center for Physics, which is supported by National Science Foundation grant PHY-2210452. Simulations were performed on PSC Bridges2 and SDSC Expanse (NSF XSEDE allocation TG-PHY160025). This research used resources of the National Energy Research Scientific Computing Center, a DOE Office of Science User Facility supported by the Office of Science of the U.S. Department of Energy under Contract No. DE-AC02-05CH11231. Computations for this research were performed on the Pennsylvania State University's Institute for Computational and Data Sciences' Roar supercomputer.

8 DATA AVAILABILITY

Simulation data will be made available upon reasonable request to the corresponding author.

REFERENCES

- Abbott B. P., et al., 2016, *Physical Review Letters*, 116, 061102
 Abbott B. P., et al., 2017, *Classical and Quantum Gravity*, 34, 044001
 Abdikamalov E. B., et al., 2010, *Physical Review D*, 81, 044012
 Ablimit I., 2022, *Monthly Notices of the Royal Astronomical Society*, 519, 1327
 Ablimit I., Podsiadlowski P., Hirai R., Wicker J., 2022, *Monthly Notices of the Royal Astronomical Society*, 513, 4802
 Arnett W. D., 1980, *The Astrophysical Journal*, 237, 541
 Arnett D., 1996, *Supernovae and Nucleosynthesis: An Investigation of the History of Matter from the Big Bang to the Present*. Princeton University Press
 Borhanian S., 2021, *Classical and Quantum Gravity*, 38, 175014
 Burrows A., Radice D., Vartanyan D., 2019, *Monthly Notices of the Royal Astronomical Society*, 485, 3153
 Caiazza I., et al., 2021, *Nature*, 595, 39
 Cappellaro E., et al., 2015, *Astronomy and Astrophysics*, 584, A62
 Centrella J. M., et al., 2001, *The Astrophysical Journal*, 550, L193
 Cerdá-Durán P., Quilis V., Font J. A., 2007, *Computer Physics Communications*, 177, 288
 Chan H., Chu M., Leung S., 2023, *The Astrophysical Journal*, 945, 133
 Chandrasekhar S., 1931a, *The London, Edinburgh, and Dublin Philosophical Magazine and Journal of Science*, 11, 592
 Chandrasekhar S., 1931b, *The Astrophysical Journal*, 74, 81
 Cheong P. C.-K., Lin L.-M., Li T. G. F., 2020, *Classical and Quantum Gravity*, 37, 145015
 Cheong P. C.-K., Lam A. T.-L., Ng H. H.-Y., Li T. G. F., 2021, *Monthly Notices of the Royal Astronomical Society*, 508, 2279
 Cheong P. C.-K., Pong D. Y. T., Yip A. K. L., Li T. G. F., 2022, *The Astrophysical Journal Supplement Series*, 261, 22
 Cheong P. C.-K., Ng H. H.-Y., Lam A. T.-L., Li T. G. F., 2023, General-relativistic radiation transport scheme in Gmnu I: Implementation of two-moment based multi-frequency radiative transfer and code tests ([arXiv:2303.03261](https://arxiv.org/abs/2303.03261))
 Chirenti C., et al., 2023, *Nature*, 613, 253
 Darbha S., Metzger B. D., Quataert E., Kasen D., Nugent P., Thomas R., 2010, *MNRAS*, 409, 846
 David Radice D., et 2019, *The Astrophysical Journal Letters*, 876, L9
 Dessart L., et al., 2006, *The Astrophysical Journal*, 644, 1063
 Dessart L., et al., 2007, *The Astrophysical Journal*, 669, 585
 Dimmelmeier H., Ott C. D., Marek A., Janka H. T., 2008, *Phys. Rev. D*, 78, 064056
 Dolence J. C., Burrows A., Zhang W., 2015, *The Astrophysical Journal*, 800, 10
 Fryer C., et al., 1999, *The Astrophysical Journal*, 516, 892
 Fuller J., et al., 2015, *Monthly Notices of the Royal Astronomical Society*, 450, 414
 Glendenning N. K., 2000, *Compact Stars*. Springer

- Gourgoulhon E., 2007, [arXiv:gr-qc/0703035](https://arxiv.org/abs/gr-qc/0703035)
- Haddadi M., et al., 2023, *Classical and Quantum Gravity*, 40, 085008
- Hammond P., Hawke I., Andersson N., 2021, *Physical Review D*, 104, 103006
- Hayama K., et al., 2018, *Monthly Notices of the Royal Astronomical Society: Letters*, 477, L96
- Hurley J. R., Tout C. A., Wickramasinghe D. T., Ferrario L., Kiel P. D., 2010, *Monthly Notices of the Royal Astronomical Society*, 402, 1437
- Kasen D., Badnell N. R., Barnes J., 2013, *The Astrophysical Journal*, 774, 25
- Kashyap R., et al., 2017, *The Astrophysical Journal*, 840, 16
- Kashyap R., et al., 2018, *The Astrophysical Journal*, 869, 140
- Kastaun W., Galeazzi F., 2015, *Physical Review D*, 91, 064027
- Khokhlov A., Mueller E., Hoefflich P., 1993, *Astronomy & Astrophysics*, 270, 223
- Klimenko S., et al., 2021, cWB pipeline library: 6.4.0, [doi:10.5281/zenodo.4419902](https://doi.org/10.5281/zenodo.4419902)
- Kuroda T., et al., 2017, *The Astrophysical Journal*, 851, 62
- Lattimer J. M., Swesty D. F., 1991, *Nuclear Physics A*, 535, 331
- Liebendörfer M., 2005, *The Astrophysical Journal*, 633, 1042
- Löffler F., et al., 2012, *Classical and Quantum Gravity*, 29, 115001
- Maggiore M., 2007, *Gravitational Waves. Vol. 1: Theory and Experiments*. Oxford Master Series in Physics, Oxford University Press
- Marek A., Janka H.-T., Müller E., 2009, *Astronomy & Astrophysics*, 496, 475
- Margalit B., Berger E., Metzger B. D., 2019, *Astrophys. J.*, 886, 110
- Metzger B. D., 2019, *Living Reviews in Relativity*, 23, 1
- Metzger B., Quataert E., Thompson T., 2008, *Monthly Notices of the Royal Astronomical Society*, 385, 1455
- Metzger B. D., et al., 2009a, *Observable Signatures of the Accretion-Induced Collapse of White Dwarfs* ([arXiv:0908.1127](https://arxiv.org/abs/0908.1127))
- Metzger B. D., Piro A. L., Quataert E., 2009b, *MNRAS*, 396, 1659
- Mezzacappa A., et al., 2022, *Core Collapse Supernova Gravitational Wave Emission for Progenitors of 9.6, 15, and 25 Solar Masses*, [doi:10.48550/ARXIV.2208.10643](https://arxiv.org/abs/2208.10643), <https://arxiv.org/abs/2208.10643>
- Mezzacappa A., et al., 2023, *Physical Review D*, 107, 043008
- Mohapatra S., et al., 2014, *Physical Review D*, 90, 022001
- Moore K., Townsley D. M., Bildsten L., 2013, *The Astrophysical Journal*, 776, 97
- Morozova V., et al., 2018, *The Astrophysical Journal*, 861, 10
- Morozova V., et al., 2020, *The Astrophysical Journal Letters*, 891, L32
- Murphy J. W., Ott C. D., Burrows A., 2009, *The Astrophysical Journal*, 707, 1173
- Müller B., Janka H.-T., 2014, *The Astrophysical Journal*, 788, 82
- Müller B., Janka H.-T., Marek A., 2013, *The Astrophysical Journal*, 766, 43
- Müller B., et al., 2017, *Monthly Notices of the Royal Astronomical Society*, 472, 491
- Nagakura H., et al., 2020, *Monthly Notices of the Royal Astronomical Society*, 500, 696
- Nakamura K., Takiwaki T., Kotake K., 2022, *Monthly Notices of the Royal Astronomical Society*, 514, 3941
- Nomoto K., 1986, *Progress in Particle and Nuclear Physics*, 17, 249
- Nomoto K., Kondo Y., 1991, *Astrophysical Journal Letters*, 367, L19
- O'Connor E. P., Couch S. M., 2018, *The Astrophysical Journal*, 854, 63
- Ott C. D., Ou S., Tohline J. E., Burrows A., 2005, *The Astrophysical Journal*, 625, L119
- Ou S., Tohline J. E., 2006, *The Astrophysical Journal*, 651, 1068
- Perego A., Bernuzzi S., Radice D., 2019, *The European Physical Journal A*, 55, 124
- Perley D., et al., 2009, *The Astrophysical Journal*, 696, 1871
- Piersanti L., et al., 2003a, *The Astrophysical Journal*, 583, 885
- Piersanti L., et al., 2003b, *The Astrophysical Journal*, 598, 1229
- Pollney D., et al., 2011, *Physical Review D*, 83, 044045
- Powell J., Müller B., 2022, *Physical Review D*, 105, 063018
- Punturo M., et al., 2010, *Classical and Quantum Gravity*, 27, 194002
- Radice D., Rezzolla L., 2012, *Astronomy & Astrophysics*, 547, A26
- Radice D., Rezzolla L., Galeazzi F., 2013, *Monthly Notices of the Royal Astronomical Society: Letters*, 437, L46
- Radice D., Rezzolla L., Galeazzi F., 2014, *Classical and Quantum Gravity*, 31, 075012
- Radice D. a., et al., 2016, *Monthly Notices of the Royal Astronomical Society*, 460, 3255
- Radice D., et al., 2018, *The Astrophysical Journal*, 869, 130
- Radice D., et al., 2022, *Monthly Notices of the Royal Astronomical Society*, 512, 1499
- Rastinejad J. C., et al., 2022, *Nature*, 612, 223
- Reisswig C., et al., 2013, *Physical Review Letter*, 111, 151101
- Roberts L. F., Reddy S., 2017, *Neutrino Signatures from Young Neutron Stars*. Springer International Publishing, Cham, pp 1605–1635, [doi:10.1007/978-3-319-21846-5_5](https://doi.org/10.1007/978-3-319-21846-5_5), https://doi.org/10.1007/978-3-319-21846-5_5
- Rodríguez M. C., et al., 2023, *Monthly Notices of the Royal Astronomical Society*, 523, 2236
- Saijo M., Yoshida S., 2006, *AIP Conference Proceedings*, 861, 728
- Saio H., Nomoto K., 2004, *The Astrophysical Journal*, 615, 444
- Schnetter E., Hawley S. H., Hawke I., 2004, *Classical and Quantum Gravity*, 21, 1465
- Shen K. J., Bildsten L., 2009, *The Astrophysical Journal*, 692, 324
- Shen K. J., Idan I., Bildsten L., 2009, *The Astrophysical Journal*, 705, 693
- Shibagaki S., et al., 2020, *Monthly Notices of the Royal Astronomical Society: Letters*, 493, L138
- Shibagaki S., et al., 2021, *Monthly Notices of the Royal Astronomical Society*, 502, 3066
- Shibata M., Baumgarte T. W., Shapiro S. L., 2000, *Astrophys. J.*, 542, 453
- Shibata M., Karino S., Eriguchi Y., 2003, *Monthly Notices of the Royal Astronomical Society*, 343, 619
- Stergioulas N., Friedman J. L., 1995, *The Astrophysical Journal*, 444, 306
- Summa A., et al., 2016, *The Astrophysical Journal*, 825, 6
- Tauris T. M., et al., 2013, *Astronomy & Astrophysics*, 558, A39
- Uenishi T., Nomoto K., Hachisu I., 2003, *The Astrophysical Journal*, 595, 1094
- Vartanyan D., et al., 2023, *The Gravitational-Wave Signature of Core-Collapse Supernovae*, [doi:10.48550/ARXIV.2302.07092](https://arxiv.org/abs/2302.07092), <https://arxiv.org/abs/2302.07092>
- Wang B., Liu D., Chen H., 2022, *Monthly Notices of the Royal Astronomical Society*, 510, 6011
- Warren M. L., Couch S. M., O'Connor E. P., Morozova V., 2020, *The Astrophysical Journal*, 898, 139
- Watts A. L., Andersson N., Jones D. I., 2004, *The Astrophysical Journal*, 618, L37
- Waxman E., 2017, *The Astrophysical Journal*, 842, 34
- Woosley S. E., et al., 2007, *The Astrophysical Journal*, 662, 487
- Yakunin K. N., et al., 2015, *Physical Review D*, 92, 084040
- Yi I., Blackman E. G., 1998, *The Astrophysical Journal*, 494, L163
- Yoon S.-C., Langer N., 2004a, *Astronomy & Astrophysics*, 419, 623
- Yoon S.-C., Langer N., 2004b, *Astronomy & Astrophysics*, 419, 645
- Yoon S. C., Langer N., 2005, *Astronomy & Astrophysics*, 435, 967

APPENDIX A: ERROR CONTROL

It is common practice in the Numerical Relativity (NR) community to present convergence tests of the simulations by showing results obtained with three different resolutions. However, numerical studies of supernova-like events usually do not present such tests. In our case, a factor 2 increase in the resolution would result in a total computational cost increase from 2.1 million to 33.6 million CPU hours. Furthermore, events such as AICs, CCSNe and SNIa are known to be turbulent and chaotic, implying that these systems are not fully deterministic. In this case, even slight changes in the grid setup may lead to changes in the evolution of the system and arbitrarily fine (and expensive) resolution schemes would be required for the convergence. This stochastic feature of supernova-like simulations has been discussed in the literature by following the shock radius for

models differing by small random density perturbations, see for example Fig. 8 of O’Connor & Couch (2018) and Fig. 17 of Summa et al. (2016).

Alternatively to the standard NR convergence tests, we follow the evolution of the Hamiltonian constraint to monitor the error in our simulations. The Hamiltonian constraint violation is defined as (Gourgoulhon 2007)

$$H \equiv {}^3D R + K^2 + K_{ij}K^{ij} - 16\pi E, \quad (\text{A1})$$

where ${}^3D R$, K_{ij} , and E are, respectively, the 3D Ricci scalar, the 3D extrinsic curvature tensor, and the matter energy density as measured by an Eulerian observer. It represents the lack of conservation of energy in our numerical evolution. Analytically, this quantity should always be zero. Numerically, the Hamiltonian constraint violation will not be trivially equal to zero and can be used as a measurement of the robustness of the numerical evolution: the smaller the violation, the more accurate the simulation is.

Our simulations presented an average Hamiltonian constraint violation below 2×10^{-5} (with a maximum value of 10^{-4} at $t = t_b$), see Fig. A1. The peak of the Hamiltonian constraint violation coincides (not by chance) with the time of bounce, when a shock wave is formed and the dynamics becomes more turbulent. The Hamiltonian constraint violation remains at higher values after the bounce due to the more complex neutrino treatment and turbulent motion in the post-bounce phase.

As previously discussed, our nrot model is consistent with previous works in the literature. Therefore, we use its Hamiltonian constraint violation as a reference value for comparison with our rotating models. All models show very similar behavior before the bounce. After the bounce, the rotating models have a higher constraint violation which does not grow further until the end of the simulations. This behavior is similar to the nrot model. These results make us confident that our simulations are numerically robust and physically meaningful and that all numerical errors are under control.

This paper has been typeset from a \LaTeX file prepared by the author.

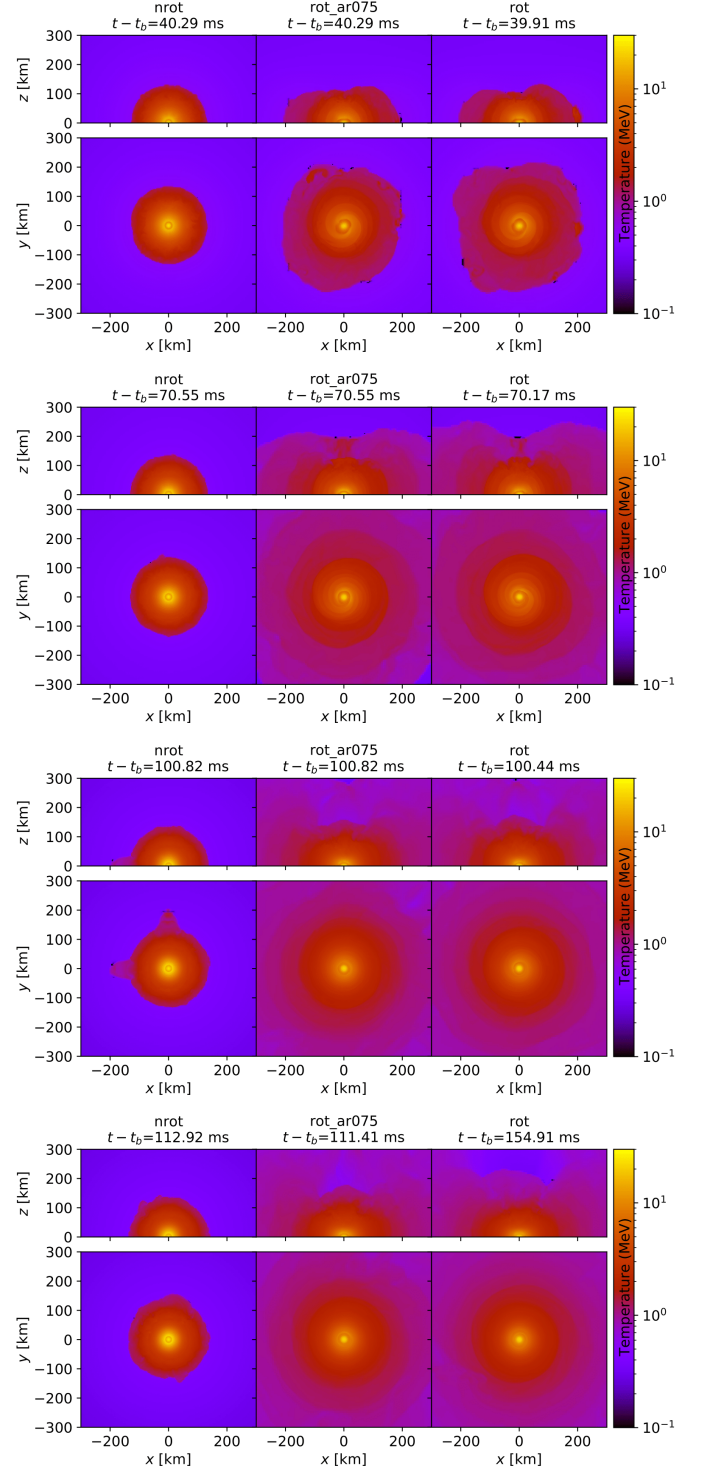


Figure 19. Temperature profiles for all our three models. Temperature is an overall decreasing function of the radius. The high-temperature material reaches larger radii due to rotation and there is a low-temperature bubble extending from the poles of the rot and rot.ar075 models.

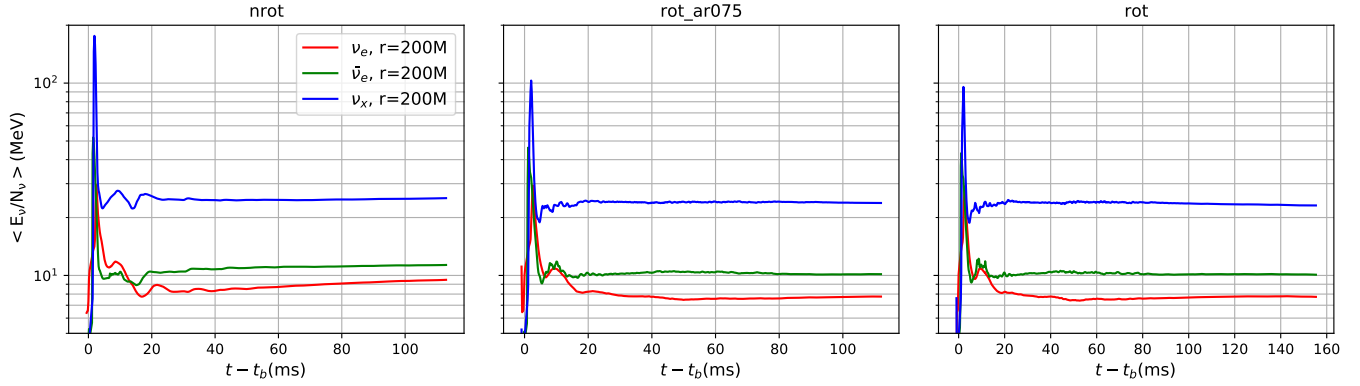


Figure 20. Average neutrino energy. Heavy lepton neutrinos are the most energetic neutrinos at all times; electron neutrinos are the least energetic. This reflects the temperature of the surface at which each neutrino flavor becomes thermally decoupled, see also Fig. 17. Rapidly rotating progenitors show lower average neutrino energies as the material is pushed to larger radii where the temperature is lower.

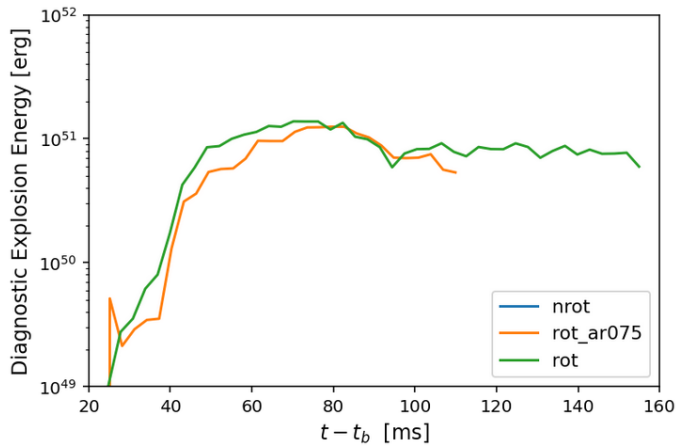


Figure 21. Diagnostic explosion energy for our three models. For the *nrot* model we find the explosion energy to be numerically consistent with zero at all times. This is consistent with the interpretation that the shock has stalled. Both models with initial angular momentum (*rot_ar075* and *rot*) have diagnostic explosion energy in the range $5-6 \times 10^{50}$ erg at the end of our simulations.

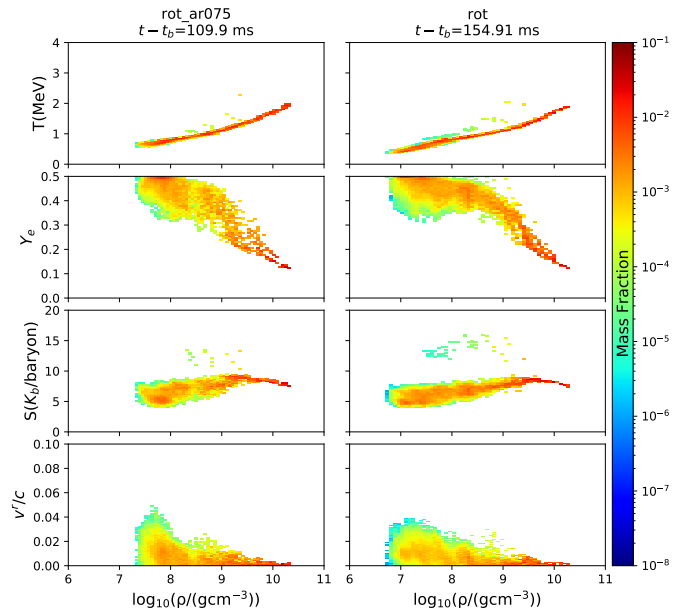


Figure 22. Snapshots of the ejecta properties as a function of density for the rotating models. (The *nrot* model presented a stalled shock and, for that reason, no ejecta was found.) The color scale shows the mass fraction normalized to the total ejecta mass, $M_{ej} \approx 3 \times 10^{-2} M_{\odot}$. First row: the tight correlation between temperature and density indicates that the ejecta material cools while it expands. Second row: the electron fraction Y_e shows a strong correlation with the density, implying that Y_e evolves as the fluid expands. For densities lower than 10^8 g/cm^3 , the value of Y_e is $\sim 0.4 - 0.5$. Third row: the entropy is almost constant over a density variation of three orders of magnitude, showing that the expansion is nearly adiabatic. Fourth row: higher velocities are found for lower density material, indicating an acceleration of the fluid during the expansion due to the explosion.

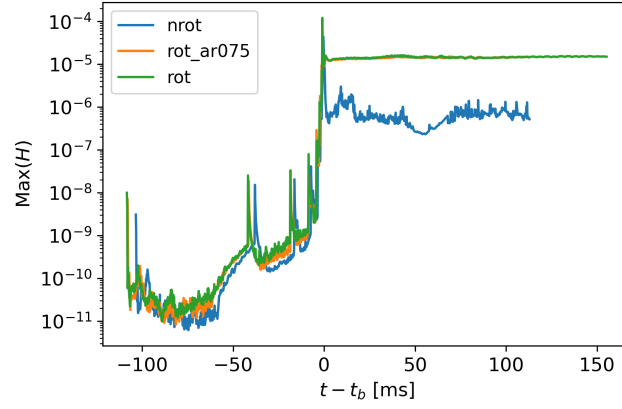


Figure A1. Maximum Hamiltonian constraint violation in our simulations. Throughout the time evolution of our models, we kept track of the Hamiltonian constraint violation. The smaller the violation, the more accurate the simulation is. Nevertheless, there is a lack of a natural scale to which these violations should be compared in order to be considered small. We use the `nrot` model as a reference and note that the violations do not grow further after the bounce, indicating the numerical stability of our code. The Hamiltonian constraint violation reaches a maximum ($\sim 10^{-4}$) near the time of bounce ($t = t_b$) due to the transition between the neutrino treatment provided by [Liebendörfer \(2005\)](#) and `WhiskyTHC`.